



# A class of deformational flow test cases for linear transport problems on the sphere<sup>☆</sup>

Ramachandran D. Nair<sup>a,\*</sup>, Peter H. Lauritzen<sup>b</sup>

<sup>a</sup> Institute for Mathematics Applied to Geosciences (IMAGe), National Center for Atmospheric Research, 1850 Table Mesa Drive, Boulder, CO 80305, USA

<sup>b</sup> Climate and Global Dynamics Division, NCAR Earth System Laboratory, National Center for Atmospheric Research, 1850 Table Mesa Drive, Boulder, CO 80305, USA

## ARTICLE INFO

### Article history:

Received 12 January 2010

Received in revised form 10 August 2010

Accepted 11 August 2010

Available online xxxx

### Keywords:

Transport scheme

Spherical geometry

Cubed-sphere

Divergent flow

Deformational flow

Discontinuous Galerkin

Semi-Lagrangian

## ABSTRACT

A class of new benchmark deformational flow test cases for the two-dimensional horizontal linear transport problems on the sphere is proposed. The scalar field follows complex trajectories and undergoes severe deformation during the simulation; however, the flow reverses its course at half-time and the scalar field returns to its initial position and shape. This process makes the exact solution available at the end of the simulation, and facilitates assessment of the accuracy of the underlying transport scheme. A procedure to eliminate possible cancellations of errors when the flow reverses is proposed.

The test suite consists of four cases. Three are based on non-divergent flow fields and one on a divergent flow. The initial conditions are prescribed in terms of regular latitude–longitude spherical coordinates and are easy to implement. The divergent flow is specifically aimed for conservative global transport schemes to test for conservation, consistency and monotonicity (or positivity) of limiters/filters in a challenging flow environment. In the context of semi-Lagrangian schemes, the time-varying flow fields can be used to test trajectory algorithms where the exact trajectories do not follow great-circle arcs. The characteristics of the test cases are demonstrated with two different transport schemes.

© 2010 Elsevier Inc. All rights reserved.

## 1. Introduction

Transport<sup>1</sup> processes are of paramount importance in atmospheric numerical modeling. Transport schemes are considered to be the basic building block of complex models. In recent years, there have been numerous efforts to develop global models based on non-conventional spherical geometry (e.g., icosahedral [1,2], cubed-sphere [3], Yin-Yang grid [4]) and advanced numerical methods (e.g., high-order finite-volume methods [5–7], continuous [8] and discontinuous Galerkin methods [9,10], radial basis functions [11,12]). Adaptive mesh refinement techniques are also gaining prominence in global modeling [13–15]. To validate and verify the numerical algorithms necessitates further development of challenging benchmark test cases. For example, recently Lauritzen et al. [16] extended the 3D idealized test case proposed by Jablonowski and Williamson [17] and found it to be useful for validating a wide range of hydrostatic atmospheric global models.

Two standard testing methods for transport schemes are the solid-body rotation and deformational flow tests. Williamson et al. [18] standardized a suite of tests for global shallow water models, including an transport problem on the sphere. They proposed the solid-body rotation of a cosine bell along a great-circle trajectory, which is perhaps the most widely used

<sup>☆</sup> The National Center for Atmospheric Research is sponsored by the National Science Foundation.

\* Corresponding author. Tel.: +1 303 497 1811; fax: +1 303 497 1286.

E-mail addresses: [rnair@ucar.edu](mailto:rnair@ucar.edu) (R.D. Nair), [pel@ucar.edu](mailto:pel@ucar.edu) (P.H. Lauritzen).

<sup>1</sup> In some literature transport and advection are used interchangeably. In order to address both divergent and non-divergent problems, we prefer to use transport instead of advection.

benchmark transport test on the sphere. Recently, Nair and Jablonowski [19] extended the static deformational flow (vortex) problem proposed by Nair and Machenhauer [20] to the “moving vortex” problem, where the vortex evolves as its center traverses along a predetermined trajectory. In both cases the evolution of the transported fields are governed by great-circle trajectories (analogous to straight lines on a Cartesian plane), facilitating easy determination of analytic solutions. While the choice of great-circle trajectories is helpful for creating idealized test cases with known analytic solutions, this may lead to test cases which are less challenging.

Two popular deformational tests in Cartesian geometry with known analytic solutions are the “Smolarkiewicz’s test” [21] and idealized cyclogenesis (also referred to as the “Doswell vortex” [22]). Staniforth et al. [23] provided the exact solution for Smolarkiewicz’s test in terms of elliptic integrals. In both cases the non-divergent deforming field (with time-independent winds) is centered at the domain’s center and symmetric with respect to an axis. For the Leveque deformational test [24] flow trajectories are much more complex. Generally, closed-form analytic solutions for the flow problems with complex trajectories are unavailable. Even if the solutions exist, they may be computationally intractable. The test [24] falls under this category. The analytic solution is only available at the end of the simulation and not at intermediate times.

Here we propose a class of deformational flow tests on the sphere following the ideas developed by Leveque [24] for a deformational test in Cartesian geometry. The initial distributions undergo severe deformation for a prescribed time, however, the flow reverses its course after the half-time and the deformed fields return to their initial states (“boomerang effect”). The trajectories of the flows are non-trivial (not along circles or straight lines) and the deformations are severe, thereby making the tests very challenging. The potential cancellation of errors due to the flow-reversal is eliminated by adding a non-divergent background flow. Contrary to the moving vortex flow fields, which has a point singularity at the center of the vortex, the wind fields in the proposed test cases are smooth and hence suitable for convergence studies. As far as we are aware there are no stand-alone divergent test cases on the sphere, and one of the proposed test cases precisely addresses that issue.

The remainder of the paper is organized as follows. Section 2 outlines deformational problem, with a brief review of the Cartesian version of the problem. Section 3 provides the details of the deformational problem on the sphere including the initial conditions. Numerical experiments and results are discussed in Section 4, followed by the conclusions.

## 2. Deformational flow problem

### 2.1. Transport equations

In the absence of sources and/or sinks, the Eulerian form of the mass continuity equation and tracer conservation equation can be written as follows:

$$\frac{\partial \rho}{\partial t} + \nabla \cdot (\rho \mathbf{V}) = 0, \quad (1)$$

$$\frac{\partial(\rho\phi)}{\partial t} + \nabla \cdot (\rho\phi \mathbf{V}) = 0, \quad (2)$$

respectively, where  $\rho$  is the fluid density and  $\mathbf{V}$  is the flow velocity vector,  $\phi$  is the tracer concentration (or mixing ratio) per unit mass so that  $\rho\phi$  may be interpreted as the tracer density [25]. We are particularly interested in the transport problem on the surface of a sphere  $\mathcal{S}$ , thus,  $\mathbf{V}$  is the 2D horizontal wind vector and ‘ $\nabla \cdot$ ’ is the divergence operator defined on  $\mathcal{S}$ . The formulations (1) and (2) are rigorously based on conservation laws (where the quantities that are conserved are  $\rho$  and  $\rho\phi$ ), and are often referred to as the flux or divergence form of the transport equation.

Eliminating  $\rho$  from (1) and (2) results in the following equation:

$$\frac{\partial \phi}{\partial t} + \nabla \cdot (\mathbf{V}\phi) = \phi \nabla \cdot \mathbf{V}. \quad (3)$$

We will refer to (3) as the *forced* transport equation for  $\phi$ . Eq. (3) can also be written in *advective form*,

$$\frac{\partial \phi}{\partial t} + \mathbf{V} \cdot \nabla \phi \equiv \frac{D\phi}{Dt} = 0, \quad (4)$$

where  $D/Dt$  corresponds to the Lagrangian (total) derivative given by

$$\frac{D}{Dt} \equiv \frac{\partial}{\partial t} + \mathbf{V} \cdot \nabla. \quad (5)$$

Eq. (4) states that  $\phi$  is preserved along Lagrangian parcel trajectories (characteristics of the flow). In the case of a non-divergent flow field,  $\nabla \cdot \mathbf{V} = 0$ , (3) reduces to the *flux-form* transport equation for  $\phi$ ,

$$\frac{\partial \phi}{\partial t} + \nabla \cdot (\phi \mathbf{V}) = 0, \quad (6)$$

(same functional form as (1) and (2)).

Note that if the flow is non-divergent and the initial condition for density is a constant  $\rho(t=0) = \rho_0$ , then the analytical solution to (1) is trivial because the initial condition is preserved at all times,  $\rho(t) = \rho_0$ . In such cases, the coupled system (1) and (2) reduces to (6) which has the same functional form (flux-form) as (2). Hence, for non-divergent flows and assuming  $\rho(t) = \rho_0$ , the transport scheme developer does not need to distinguish between tracer density  $\rho\phi$  and mixing ratio  $\phi$  as they are interchangeable (at least in the continuous case). This is the configuration implicitly assumed in most (if not all) idealized transport test cases on the sphere that have been proposed in the meteorological literature.

We also note that if the mass continuity Eq. (1) and tracer Eq. (2) are solved in flux-form, then (2) trivially reduces to (1) when  $\phi = 1$ . This should ideally also be the case in the numerical implementation of transport schemes and is referred to as the *mass-wind* consistency in meteorological literature (e.g., [26,27]).

Conservative Eulerian transport schemes rely on the flux-form formulation, while non-conservative transport schemes usually employ the advective form (4). However, for conservative semi-Lagrangian transport the integral form of the conservation laws are used [28,27].

## 2.2. Deformational problem in Cartesian geometry

In this study the main focus is the deformational flow on the sphere, nevertheless, we briefly review the original Cartesian formulation of the problem discussed in [24]. For the deformational flow field the time dependent velocity vector is defined as follows:

$$\mathbf{V}(x, y, t) = \mathbf{v}(x, y)\varphi(t),$$

where  $\varphi(t)$  is the time-dependent function and its magnitude monotonically decreases and reaches zero at half-time and then increases with a sign change, resulting in a reversal of the flow field  $\mathbf{V}$ . Leveque [24] diligently choose  $\varphi(t) = \cos(\pi t/T)$ , where  $T$  is the final time of the evolution (integration) such that  $0 \leq t \leq T$ . As discussed in [23], there is a limiting time beyond which it is no longer possible to represent all the spatial scales because the length scale of the exact solution diminishes as a function of time. Thus, the choice of  $T$  for deformational flow should be meaningful in such a way that length scales should be adequately resolvable.

In Cartesian geometry, the components of velocity ( $u, v$ ) may be specified as follows:

$$u(x, y, t) = \sin^2(\pi x) \sin(2\pi y) \cos(\pi t/T), \quad (7)$$

$$v(x, y, t) = -\sin^2(\pi y) \sin(2\pi x) \cos(\pi t/T), \quad (8)$$

where  $0 \leq x, y \leq 1$ , and the final time  $T = 5$  units [29]. At the initial time let  $u(x, y, t=0) = u_0(x, y)$  and  $v(x, y, t=0) = v_0(x, y)$ , then the stream function is

$$\psi = -\frac{1}{\pi} \sin^2(\pi x) \sin^2(\pi y), \quad (9)$$

such that  $\partial\psi/\partial x = v_0(x, y)$  and  $\partial\psi/\partial y = -u_0(x, y)$ . Clearly the flow fields defined by (7) and (8) are non-divergent ( $\nabla \cdot \mathbf{v} = \partial u/\partial x + \partial v/\partial y = 0$ ). The trajectories which follow the fluid motion are given by a coupled system of ordinary differential equations (kinematic equations):

$$\frac{dx}{dt} = u(x, y, t), \quad (10)$$

$$\frac{dy}{dt} = v(x, y, t). \quad (11)$$

The initial values for the transported scalar field  $\phi$  in (4) or (6) may be a quasi-smooth function in a unit square domain. Durran [29] employs a cosine bell as the initial distribution for  $\phi$  and is defined as follows:

$$\phi(x, y) = \frac{1}{2} [1 + \cos(\pi R)], \quad R = \min \left\{ 1, 4[(x - 1/4)^2 + (y - 1/4)^2]^{1/2} \right\}.$$

The extreme deformation for  $\phi$  during the evolution occurs at  $t = T/2$ , and  $\phi$  recovers its initial values at  $t = T$ . When  $t = T/2$  the initial circular pattern of the cosine bell deforms to a narrow stretched band as shown in [29].

Discrete numerical schemes representing transport Eqs. (4) and (6) can be validated by using the above initial conditions. Also, this provides a challenging test case for experimenting with monotonic and positivity preserving limiters/filters in transport schemes [30]. Note that the Eulerian transport schemes rely on time-dependent wind fields (7) and (8), while semi-Lagrangian (SL) schemes based on the discretization of  $D\phi/Dt = 0$  in (4) require explicit knowledge of the trajectories (10) and (11). A detailed discussion of conservative SL methods can be found in [31,27]. As noted in [32], a potential weakness of this test is that the phase errors for each Fourier mode could partially cancel when the flow reverses. Nevertheless, the cancellation of errors can be avoided by choosing a different flow path (trajectory) when the flow returns after the half-time. We provide a simple procedure to address this issue in the next section.

The unavailability of an exact solution is not a serious drawback because by design the final solution  $\phi(t = T)$  is known and is identical to the initial condition  $\phi(t = 0)$ . The accuracy of the underlying transport schemes can be validated by computing standard error norms and mass errors at the final step of the integration ( $t = T$ ).

### 3. Specification of the problem in spherical geometry

We provide four sets of velocity fields  $\mathbf{V}(\lambda, \theta, t)$  on the sphere with longitude  $\lambda$  and latitude  $\theta$  such that  $0 \leq \lambda \leq 2\pi$  and  $-\pi/2 \leq \theta \leq \pi/2$ . For simplicity, we assume that the radius  $R$  of the sphere is one. The velocity fields are prescribed for both divergent and non-divergent flows, mimicking different flow situations found in practical applications. For the proposed tests, the duration of integration is  $T = 5$  units and we assume a constant initial density field  $\rho(t = 0) = 1$ . The spatial distributions for the tracer mixing ratio (or concentration)  $\phi$  at  $t = 0$  are given below.

#### 3.1. Initial scalar fields $\phi$

We use three different initial conditions. First of all one based on the quasi-smooth cosine-bell pattern (a  $C^1$  function) that is widely used for the solid-body rotation test [18]. Second, one based on smooth Gaussian profiles ( $C^\infty$ ) which may be used for convergence studies (in particular when using high-order schemes<sup>2</sup>) under challenging flow environments. The quasi-smooth profiles may be used for checking monotonicity (non-oscillatory property), however, we also use a more challenging pattern based on a slotted-cylinder distribution (a discontinuous function). In order to take advantage of the symmetry of the flow on the spherical domain  $\mathcal{S}$ , two identical scalar distributions (patterns) are created at selected points. This could help debugging (or testing for errors) numerical schemes and/or spherical grid-systems by checking for symmetry in the flow fields and the distributions. The deforming profiles are expected to keep the symmetry during the entire evolution cycle.

##### 3.1.1. Quasi-smooth scalar field

Two symmetrically located cosine bells are defined as follows,

$$h_i(\lambda, \theta) = \frac{h_{\max}}{2} [1 + \cos(\pi r_i / r)] \quad \text{if } r_i < r, \quad (12)$$

where  $h_{\max} = 1$ ,  $r = 1/2$  is the base radius of the bells,  $r_i = r_i(\lambda, \theta)$  is the great-circle distance between  $(\lambda, \theta)$  and a specified center  $(\lambda_i, \theta_i)$  of the cosine bell, which is given by

$$r_i(\lambda, \theta) = \arccos[\sin \theta_i \sin \theta + \cos \theta_i \cos \theta \cos(\lambda - \lambda_i)].$$

The initial condition  $\phi$  consists of a background value  $b$  and two cosine bells with centers  $(\lambda_1, \theta_1)$  and  $(\lambda_2, \theta_2)$ , respectively, generated using (12)

$$\phi(\lambda, \theta) = \begin{cases} b + c h_1(\lambda, \theta) & \text{if } r_1 < r, \\ b + c h_2(\lambda, \theta) & \text{if } r_2 < r, \\ b & \text{otherwise,} \end{cases} \quad (13)$$

where the parameters are  $b = 0.1$  and  $c = 0.9$  such that the values of  $\phi \in [0.1, 1.0]$ . This choice allows the background value  $b$  of  $\phi$  to be non-zero. In general, a non-zero background field is more challenging for the transport scheme. However, for the positivity test zero background values are more suitable and it can be easily set by choosing  $b = 0$  and  $c = 1$  in (13) such that  $\phi \in [0, 1]$ . Also, for the non-divergent test cases using a non-zero constant distribution (e.g.,  $b = 1, c = 0$ ) is a non-trivial test to assess a transport scheme's ability to preserve a constant  $\phi$ -field throughout the simulation. The scheme's ability to preserve a constant density field  $\rho$  could be tested the same way.

##### 3.1.2. Smooth scalar field

Smooth 2D Gaussian surfaces can be defined on  $\mathcal{S}$  using the following relation:

$$h_i(\lambda, \theta) = h_{\max} \exp \left\{ -b_0 [(X - X_i)^2 + (Y - Y_i)^2 + (Z - Z_i)^2] \right\}, \quad (14)$$

where  $h_{\max} = 1$  is the height of the Gaussian hill and  $b_0 = 5$  defines the width [34].  $(X, Y, Z)$  are the 3D absolute Cartesian coordinates corresponding to the spherical  $(\lambda, \theta)$  coordinates and are related through

$$(X, Y, Z) = (R \cos \theta \cos \lambda, R \cos \theta \sin \lambda, R \sin \theta), \quad (15)$$

where radius  $R = 1$  (unit sphere). The center of the Gaussian distribution  $(X_i, Y_i, Z_i)$  can be specified in terms of  $(\lambda_i, \theta_i)$  using (15). This field is infinitely smooth ( $C^\infty$ ).

<sup>2</sup> As an example, [33] found sub-optimal numerical convergence rates for the solid-body transport problem when using the  $C^1$  cosine bell initial condition; with their  $C^3$ -version of the cosine bell higher-order numerical convergence rates were indeed observed.

As in the case of the cosine bells, we create two Gaussian hills for the initial scalar distribution  $\phi$  as the sum of two fields  $h_1$  and  $h_2$  using (14),

$$\phi(\lambda, \theta) = h_1(\lambda, \theta) + h_2(\lambda, \theta). \quad (16)$$

### 3.1.3. Non-smooth scalar field

To test for monotonicity (or non-oscillatoriness), a non-smooth initial scalar distribution may be used. The *slotted-cylinder* transport problem on the Cartesian plane [35] provides an excellent test case for monotonicity preservation and can easily be adopted for spherical geometry applications [36]. For the non-smooth case, the double cosine-bells (13) are replaced by slotted-cylinders defined as follows:

$$\phi(\lambda, \theta) = \begin{cases} c & \text{if } r_i \leq r \text{ and } |\lambda - \lambda_i| \geq r/6 \text{ for } i = 1, 2, \\ c & \text{if } r_1 \leq r \text{ and } |\lambda - \lambda_1| < r/6 \text{ and } \theta - \theta_1 < -\frac{5}{12}r, \\ c & \text{if } r_2 \leq r \text{ and } |\lambda - \lambda_2| < r/6 \text{ and } \theta - \theta_2 > \frac{5}{12}r, \\ b & \text{otherwise,} \end{cases} \quad (17)$$

where  $c = 1$  and  $b = 0.1$ . Note that the slots are oriented in opposite directions for the two cylinders so that they are symmetric with respect to the flow.

## 3.2. Initial wind fields

The test cases are controlled by the parameters  $k$ , the amplitude of the flow fields, and the centers of the initial distributions  $(\lambda_i, \theta_i)$ , where  $i = 1, 2$ . The values for  $k$  and  $(\lambda_i, \theta_i)$  are particularly chosen to make the test cases challenging. The components of the velocity vector  $\mathbf{V}(\lambda, \theta, t)$  (and stream functions for the non-divergent cases) and the initial positions of the distributions,  $(\lambda_i, \theta_i)$  with  $i = 1, 2$ , are defined below.

### 3.2.1. Non-divergent flows

- Case-1:

$$u(\lambda, \theta, t) = k \sin^2(\lambda/2) \sin(2\theta) \cos(\pi t/T), \quad (18)$$

$$v(\lambda, \theta, t) = \frac{k}{2} \sin(\lambda) \cos(\theta) \cos(\pi t/T), \quad (19)$$

$$\psi(\lambda, \theta, t) = k \sin^2(\lambda/2) \cos^2(\theta) \cos(\pi t/T), \quad (20)$$

where  $\psi$  is the stream function

$$u = -\frac{\partial \psi}{\partial \theta}, \quad (21)$$

$$v = \frac{1}{\cos \theta} \frac{\partial \psi}{\partial \lambda}. \quad (22)$$

The flow parameter  $k$  is set to 2.4. Initially, the centers of the distributions (cosine bells, slotted cylinders or Gaussian hills) are kept at  $(\lambda_1, \theta_1) = (\pi, \pi/3)$  and  $(\lambda_2, \theta_2) = (\pi, -\pi/3)$ , respectively. Initial wind fields and Cosine bell distributions are shown in Fig. 1a and b, respectively.

- Case-2:

$$u(\lambda, \theta, t) = k \sin^2(\lambda) \sin(2\theta) \cos(\pi t/T), \quad (23)$$

$$v(\lambda, \theta, t) = k \sin(2\lambda) \cos(\theta) \cos(\pi t/T), \quad (24)$$

$$\psi(\lambda, \theta, t) = k \sin^2(\lambda) \cos^2(\theta) \cos(\pi t/T), \quad (25)$$

where the parameter  $k = 2$ . Initial positions of the centers of the distributions are at  $(\lambda_1, \theta_1) = (5\pi/6, 0)$  and  $(\lambda_2, \theta_2) = (7\pi/6, 0)$ , respectively. For Case-2, Fig. 2a and b show the wind fields as well as the initial distribution (in this case cosine-bell) positions.

The above flow fields defined by Eq.(18) and (19) and (23) and (24) are non-divergent because

$$\nabla \cdot \mathbf{V} = \frac{1}{\cos \theta} \left[ \frac{\partial u}{\partial \lambda} + \frac{\partial (v \cos \theta)}{\partial \theta} \right] = 0.$$

### 3.2.2. Divergent flow

This wind field is proposed, in particular, for conservative transport schemes which are supposed to preserve total mass even in divergent flows on a closed domain such as the sphere. It also provides a challenging flow-environment to test

## Deformational Flow (DG3): Case-1, CB

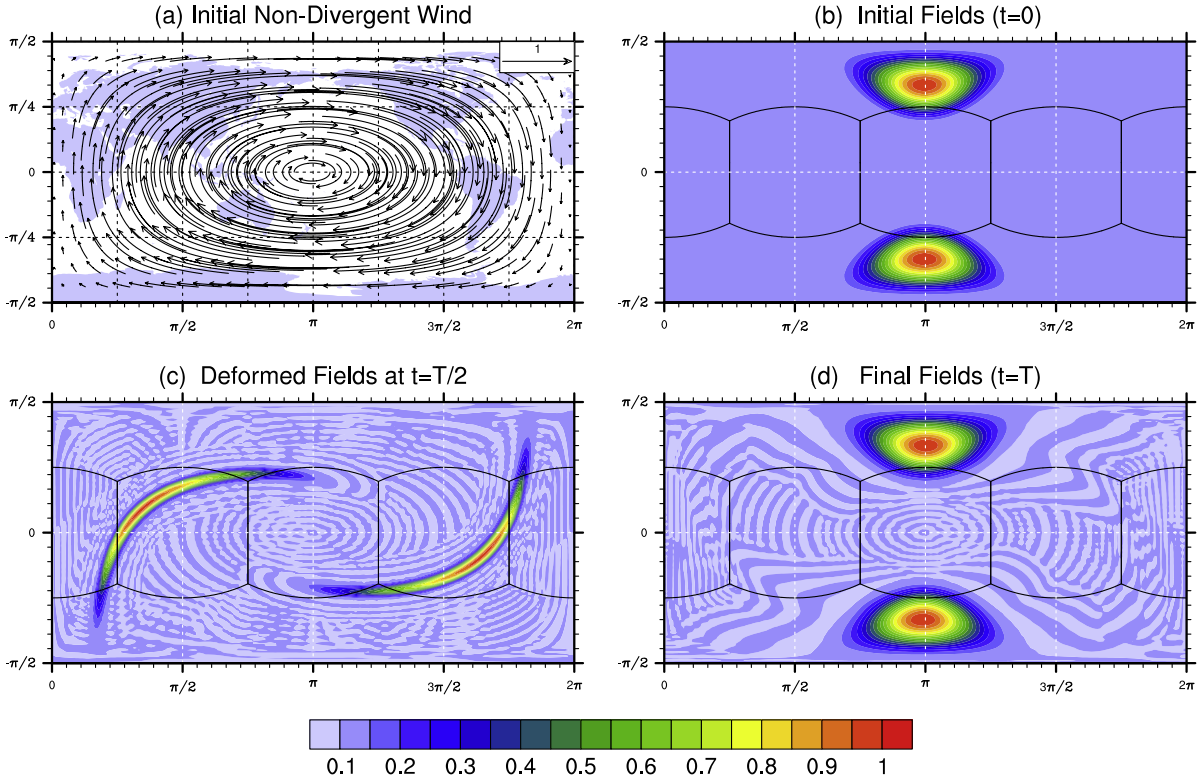


**Fig. 1.** The non-divergent deformational flow test case 1 at an approximate resolution of 1.5° along the equator. (a) Initial wind field and (b) initial scalar fields  $\phi(t=0)$  (cosine-bells with centers at  $(\pi, \pi/3)$  and  $(\pi, -\pi/3)$ , respectively). (c) Numerical solution for  $\rho\phi$  at time  $t = T/2$  units computed with a third-order DG transport scheme. (d) Numerical solution for  $\rho\phi$  at  $t = T$  when the cosine-bell patterns return back to their initial positions.

limiters/filters under divergent flow conditions. Most global idealized transport test cases in the literature 'only' consider non-divergent flows.

- Case-3:

$$u(\lambda, \theta, t) = -k \sin^2(\lambda/2) \sin(2\theta) \cos^2(\theta) \cos(\pi t/T), \quad (26)$$

$$v(\lambda, \theta, t) = \frac{k}{2} \sin(\lambda) \cos^3(\theta) \cos(\pi t/T), \quad (27)$$

where  $k = 1$ , and the centers of the distributions are at  $(\lambda_1, \theta_1) = (3\pi/4, 0)$  and  $(\lambda_2, \theta_2) = (5\pi/4, 0)$ , respectively. The initial divergent wind and initial positions of the distributions (cosine bells) are shown in Fig. 3a and b, respectively.

All the flow fields defined above do not have cross-polar flow. For transport schemes developed on the regular latitude-longitude sphere, the cross-polar transport is a major challenge. However, the above-defined wind fields can be prescribed in rotated spherical coordinates  $(\lambda', \theta')$  with respect to regular  $(\lambda, \theta)$ -system, so that the flow can be oriented in any desired direction [19] and the transport scheme in question can be tested.

### 3.2.3. Zonal background flow

As mentioned earlier, there is a possibility of cancellations of errors due to reversal of the flow along the same trajectories (flow path) after the half-time  $T/2$ . This can be avoided by introducing different trajectories after time  $T/2$ . A zonal non-divergent background flow (as used for the solid-body rotation case [18]) will precisely address this issue without affecting the structure of the deformations [19]. The zonal wind will translate the deforming fields as a whole along the zonal direction which effectively introduces new trajectories after the flow reversal at time  $T/2$ . In practice, this can be done by prescribing the deformational velocity fields  $\mathbf{V}(\lambda, \theta, t)$  in rotated coordinates  $(\lambda', \theta')$  with respect to the regular  $(\lambda, \theta)$  coordinates. Rotation is time dependent and may be synchronized with the new zonal solid-body velocity component  $u'(\theta)$  which should be added to  $\mathbf{V}$ .

The rotated system is defined as

$$(\lambda', \theta') = (\lambda - \omega' t, \theta); \quad \omega' = \frac{d\lambda}{dt}, \quad (28)$$

## Deformational Flow (DG3): Case-2, CB

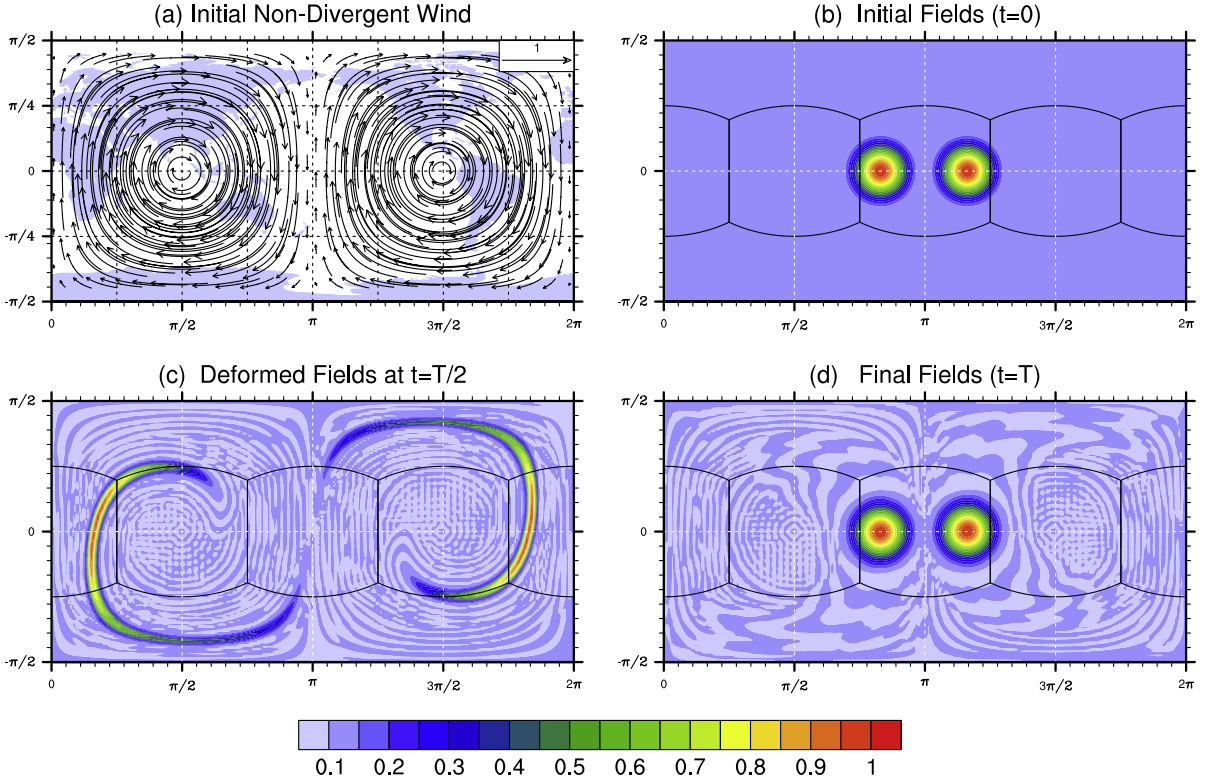


Fig. 2. Same as in Fig. 1 but for a different non-divergent deformational flow field (Case-2).

where  $\omega'$  is the angular velocity associated with the rotation along the zonal direction (i.e., with respect to the north–south axis of the  $(\lambda, \theta)$  system). The value of  $\omega'$  may be chosen as  $\omega' = 2\pi/T$ , so that a complete revolution is made at time  $t = T$ . This is also the total time used for the deformational flow itself. The zonal solid-body velocity is chosen to be  $u'(\theta) = \omega' \cos \theta$ . In brief, the resultant (effective) velocity fields  $(u_e, v_e)$  due to the solid-body zonal velocity and deformational velocity can be written as follows:

$$u_e(\lambda, \theta, t) = u(\lambda', \theta, t) + u'(\theta), \quad (29)$$

$$v_e(\lambda, \theta, t) = v(\lambda', \theta, t). \quad (30)$$

The effective velocity fields  $(u_e, v_e)$  corresponding to the deformational flows (Case 1–3) can be easily derived using (29) and (30).

For example, we combine the solid-body velocity with the deformational velocity used in Case-2 to form an effective velocity. The initial positions of the distributions (cosine-bells, Gaussian hills or slotted cylinders) and other parameters are exactly as given in Case-2. This case is referred to as “Case-4”.

- Case-4:

$$u_e(\lambda, \theta, t) = k \sin^2(\lambda') \sin(2\theta) \cos(\pi t/T) + 2\pi \cos(\theta)/T, \quad (31)$$

$$v_e(\lambda, \theta, t) = k \sin(2\lambda') \cos(\theta) \cos(\pi t/T), \quad (32)$$

$$\psi(\lambda, \theta, t) = k \sin^2(\lambda') \cos^2(\theta) \cos(\pi t/T) - 2\pi \sin(\theta)/T, \quad (33)$$

where  $\lambda' = \lambda - 2\pi t/T$  (see Fig. 4(a–b)).

Note that for the Cases 1–4, the wind field and initial scalar distributions are defined in non-dimensional units. This choice is for broader application of the test cases across different disciplines where the transport problem on a sphere is important. However, it is possible to adapt the problem for a particular application by choosing meaningful scaling factors (dimensional units). In atmospheric modeling, for example, the radius of the sphere  $R$  would be the mean radius of the earth. Based on that a suitable length scale can be introduced. The time scale may be changed to  $T = 12$  days for a complete revolution around the earth [18]. The parameter  $k$  may be redefined to have dimensional units as used in [19]. For an example of an ‘atmospheric’ scaling of test case 2 see [33].

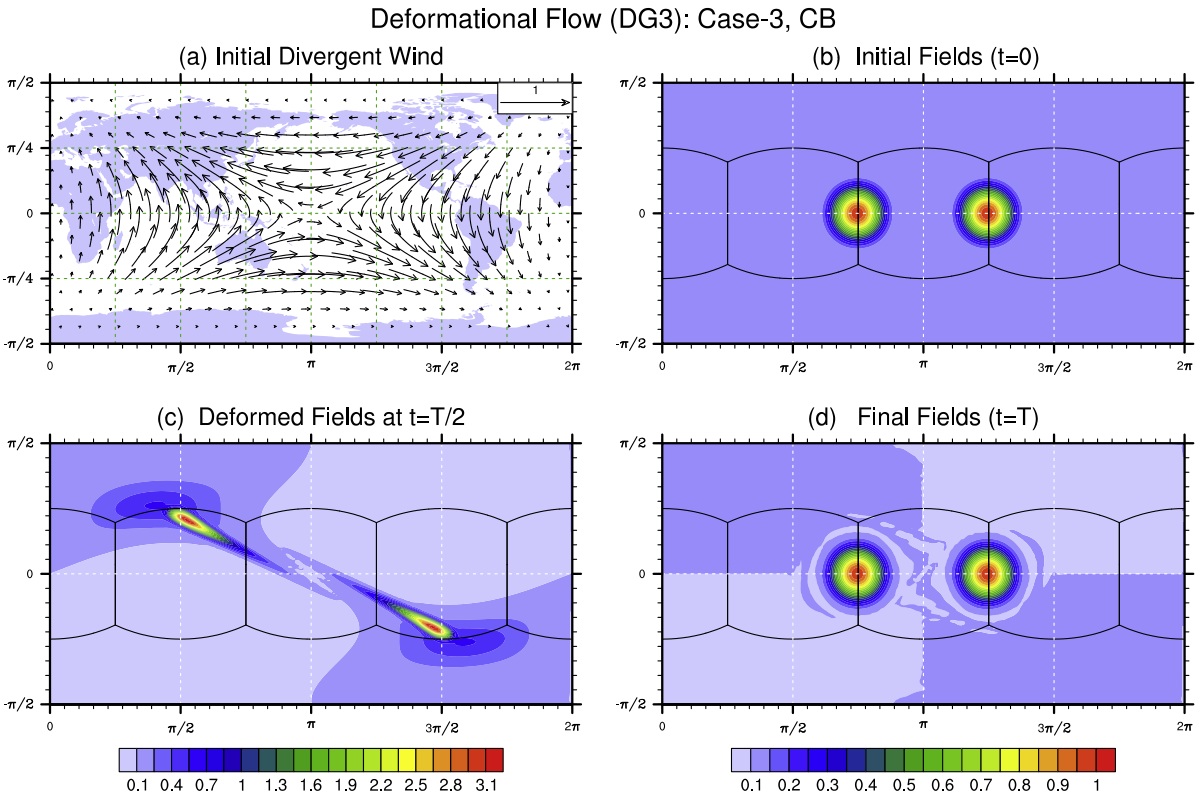


Fig. 3. Same as Fig. 1 but for the divergent deformational flow field (Case-3).

### 3.3. Approximate trajectories for semi-Lagrangian transport

Semi-Lagrangian transport schemes require upstream trajectory information (or the departure point positions) at every time step, which can be obtained by solving the ordinary differential equations (10) and (11). In practical applications such as global atmospheric models usually second-order accurate ( $\mathcal{O}[(\Delta t)^2]$ ) numerical trajectories are computed using an iterative algorithm as the one given in [37]. Standard Runge-Kutta methods can, of course, also be used (e.g., [38]). Since the analytical velocity fields are known for the test cases considered herein, an alternative high-order option based on Taylor series expansions is available [36], that is, the upstream position of  $\mathbf{x}_d$  at the departure time  $t - \Delta t$  is given by,

$$\mathbf{x}_d \equiv \mathbf{x}(t - \Delta t) = \mathbf{x}(t) - \Delta t \frac{d}{dt} \mathbf{x}(t) + \frac{(\Delta t)^2}{2!} \frac{d^2}{dt^2} \mathbf{x}(t) - \dots, \quad (34)$$

where the wind vector is  $\mathbf{V} = d\mathbf{x}(t)/dt$ .

As an example we consider the Case-1 non-divergent wind (i.e., Eqs. (18) and (19)), for which the upstream position  $(\lambda_d, \theta_d)$  can be easily determined. From (18) and (19),

$$\begin{aligned} \frac{d\lambda}{dt} &= \frac{u}{\cos \theta} = 2k \sin^2(\lambda/2) \sin(\theta) \cos(\omega t), \\ \frac{d\theta}{dt} &= v = \frac{k}{2} \sin(\lambda) \cos(\theta) \cos(\omega t), \end{aligned}$$

where  $\omega = \pi/T$ . By using (34) and the above relations, an  $\mathcal{O}[(\Delta t)^3]$  accurate approximation can be derived for  $\lambda(t - \Delta t)$  and  $\theta(t - \Delta t)$ :

$$\begin{aligned} \lambda_d &= \lambda(t - \Delta t) \approx \lambda - \Delta t \tilde{u} - (\Delta t)^2 k \sin\left(\frac{\lambda}{2}\right) \left\{ \sin\left(\frac{\lambda}{2}\right) \sin(\theta) \sin(\omega t) \omega - \tilde{u} \sin(\theta) \cos(\omega t) \cos\left(\frac{\lambda}{2}\right) \right. \\ &\quad \left. - v \sin\left(\frac{\lambda}{2}\right) \cos(\theta) \cos(\omega t) \right\}, \end{aligned} \quad (35)$$

$$\theta_d = \theta(t - \Delta t) \approx \theta - \Delta t v - \frac{(\Delta t)^2}{4} k \{ \sin(\lambda) \cos(\theta) \sin(\omega t) \omega - \tilde{u} \cos(\lambda) \cos(\theta) \cos(\omega t) + v \sin(\lambda) \sin(\theta) \cos(\omega t) \}, \quad (36)$$

where

## Deformational Flow + SB (DG3): Case-4, CB

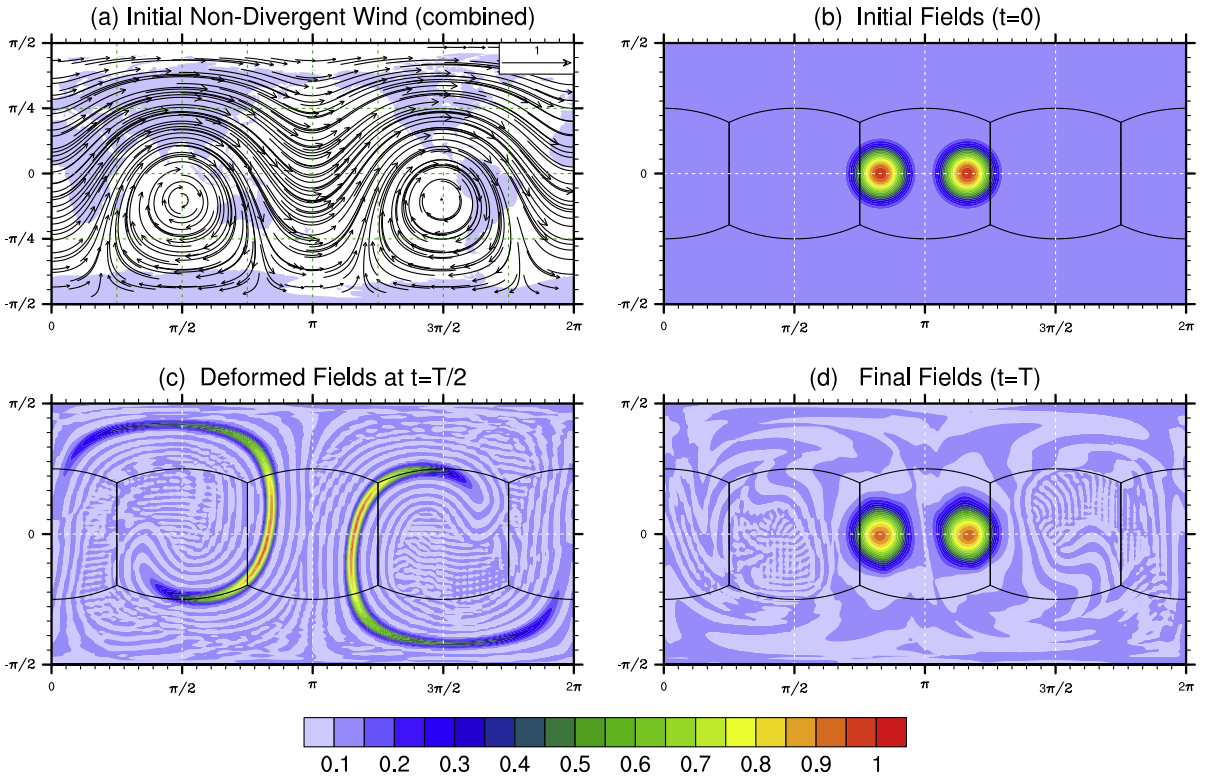


Fig. 4. Same as in Fig. 2 but with a zonal background flow.

$$\tilde{u} \equiv \frac{d\lambda}{dt} = \frac{u(\lambda, \theta, t)}{\cos(\theta)} = 2k \sin^2(\lambda/2) \sin(\theta) \cos(\pi t/T) \quad (37)$$

and the velocity components  $u$  and  $v$  are given in (18) and (19), respectively. All terms on the right-hand side of (35) and (36) are evaluated at the arrival point  $(\lambda(t), \theta(t))$  at time  $t$ .

For all the remaining Cases (2–4), the third-order accurate upstream trajectory origins (departure points)  $(\lambda_d, \theta_d)$  can be derived similarly:

- For Case-2:

$$\lambda_d = \lambda(t - \Delta t) \approx \lambda - \Delta t \tilde{u} - (\Delta t)^2 k \sin(\lambda) \{ \sin(\lambda) \sin(\omega t) \omega \sin(\theta) - 2\tilde{u} \cos(\omega t) \cos(\lambda) \sin(\theta) - v \sin(\lambda) \cos(\omega t) \cos(\theta) \} \quad (38)$$

$$\theta_d = \theta(t - \Delta t) \approx \theta - \Delta t v - (\Delta t)^2 k \{ \cos(\theta) \sin(\omega t) \omega \sin(\lambda) \cos(\lambda) - 2\tilde{u} \cos(\theta) \cos(\omega t) (\cos(\lambda))^2 + \tilde{u} \cos(\theta) \cos(\omega t) + v \sin(\theta) \cos(\omega t) \sin(\lambda) \cos(\lambda) \}. \quad (39)$$

- For Case-3:

$$\begin{aligned} \lambda_d = \lambda(t - \Delta t) \approx \lambda - \Delta t \tilde{u} + (\Delta t)^2 \sin\left(\frac{\lambda}{2}\right) k \cos(\theta) \left\{ \sin\left(\frac{\lambda}{2}\right) \sin(\omega t) \omega \cos(\theta) \sin(\theta) - \tilde{u} \cos(\omega t) \cos(\theta) \cos\left(\frac{\lambda}{2}\right) \sin(\theta) \right. \\ \left. - 3v \sin\left(\frac{\lambda}{2}\right) \cos(\omega t) (\cos(\theta))^2 + 2v \sin\left(\frac{\lambda}{2}\right) \cos(\omega t) \right\} \end{aligned} \quad (40)$$

$$\begin{aligned} \theta_d = \theta(t - \Delta t) \\ \approx \theta - \Delta t v - \frac{(\Delta t)^2}{4} k (\cos(\theta))^2 \{ \sin(\lambda) \cos(\theta) \sin(\omega t) \omega - \tilde{u} \cos(\lambda) \cos(\theta) \cos(\omega t) + 3v \sin(\lambda) \cos(\omega t) \sin(\theta) \}. \end{aligned} \quad (41)$$

- For Case-4:

$$\begin{aligned}\lambda_d &= \lambda(t - \Delta t) \\ &\approx \lambda - \Delta t \tilde{u}' - (\Delta t)^2 k \sin(\lambda') \{ \sin(\lambda') \sin(\omega t) \omega \sin(\theta) - 2 \tilde{u}' \cos(\omega t) \cos(\lambda') \sin(\theta) - v' \sin(\lambda') \cos(\omega t) \cos(\theta) \},\end{aligned}\quad (42)$$

$$\begin{aligned}\theta_d &= \theta(t - \Delta t) \approx \theta - \Delta t v' - (\Delta t)^2 k \{ \cos(\theta) \sin(\omega t) \omega \sin(\lambda') \cos(\lambda') - 2 \tilde{u}' \cos(\theta) \cos(\omega t) (\cos(\lambda'))^2 \\ &\quad + \tilde{u}' \cos(\theta) \cos(\omega t) + v' \sin(\theta) \cos(\omega t) \sin(\lambda') \cos(\lambda') \},\end{aligned}\quad (43)$$

where

$$\tilde{u}' \equiv \frac{u_e(\lambda, \theta, t)}{\cos(\theta)} = 2 k \sin^2(\lambda') \sin(\theta) \cos(\pi t/T) + \omega' \quad (44)$$

and

$$v' = k \sin(2\lambda') \cos(\theta) \cos(\pi t/T). \quad (45)$$

Note that there are no singular points for  $u$  or  $v$  in any of the Taylor series expansions for any of the test cases. As a result, the departure point position is “well behaved” near the poles. The Taylor series approach outlined above assumes upstream trajectories. However, it may easily be modified for downstream trajectories.

### 3.4. Accurate trajectory computation

Higher-order trajectories can be computed by including more terms in the Taylor series expansions at the cost that the expressions for the departure points get longer and more cumbersome to code as the order is increased. Alternatively, more accurate trajectories can be obtained by splitting the trajectory into segments where each segment is computed using the Taylor series expansion method. This can be easier to code than introducing more terms in the Taylor series expansion. In this case, the trajectory is split into  $m$  segments, and each segment corresponds to a displacement during the fractional time step  $\Delta\tau = \Delta t/m$ . The  $m$  trajectory segments are given by:

$$\begin{aligned}\mathbf{x}_0 &\equiv \mathbf{x}(t), \\ \mathbf{x}_1 &\equiv \mathbf{x}(t - \Delta\tau) = \mathbf{x}_0 - (\Delta\tau) \frac{d}{dt} \mathbf{x}_0 + \frac{(\Delta\tau)^2}{2!} \frac{d^2}{dt^2} \mathbf{x}_0 - \dots, \\ \mathbf{x}_2 &\equiv \mathbf{x}(t - 2\Delta\tau) = \mathbf{x}_1 - (\Delta\tau) \frac{d}{dt} \mathbf{x}_1 + \frac{(\Delta\tau)^2}{2!} \frac{d^2}{dt^2} \mathbf{x}_1 - \dots, \\ &\vdots \quad \vdots \\ \mathbf{x}_m &\equiv \mathbf{x}(t - \Delta t) = \mathbf{x}_{m-1} - (\Delta\tau) \frac{d}{dt} \mathbf{x}_{m-1} + \frac{(\Delta\tau)^2}{2!} \frac{d^2}{dt^2} \mathbf{x}_{m-1} - \dots,\end{aligned}\quad (46)$$

where  $\mathbf{x}(t) = (\lambda(t), \theta(t))$ . The last segment (46) leads to the departure point  $\mathbf{x}_d = \mathbf{x}_m = \mathbf{x}(t - \Delta t)$ .

For example, the trajectories for Case-1 are computed as follows. The algorithm is initialized with the arrival point  $\mathbf{x}_0 \equiv \mathbf{x}(t) = (\lambda(t), \theta(t))$ . Then, the first segment is computed exactly as explained in the previous Section using the Taylor series method, i.e. by evaluating (35) and (36) at  $\mathbf{x}_0$  but replacing  $\Delta t$  with the fractional time-step  $\Delta\tau$ . This yields the intermediate departure point  $\mathbf{x}_1$ . The next segment is computed, again, with the Taylor series approach (Eq. (35) and (36)) but the terms in the Taylor series are evaluated at the intermediate departure point  $\mathbf{x}_1$  at time  $t - \Delta\tau$  (again replacing  $\Delta t$  with  $\Delta\tau$  in the Taylor series expansions). This leads to the second intermediate departure point  $\mathbf{x}_2$ . The third segment is computed by evaluating the terms in the Taylor series expansion at the previous intermediate departure point  $\mathbf{x}_2$  at  $t - 2\Delta\tau$ . This leads to the second intermediate departure point  $\mathbf{x}_2$ . This process is repeated  $m$  times. Fig. 5 schematically depicts the trajectory segments for  $m = 3$ , connecting the departure point  $\mathbf{x}(t - \Delta t)$  and the arrival point  $\mathbf{x}(t)$ .

## 4. Numerical experiments

We demonstrate numerical simulations with the four deformational tests (Cases 1–4) that were defined in the previous section. The two transport schemes employed are based on a discontinuous Galerkin (DG) method and a conservative SL method, respectively. Both schemes use the cubed-sphere spherical domain [39,3]. The choice for the spherical grid system (domain) and transport schemes is quite arbitrary, and any spherical transport scheme could be used for the demonstration. The reason for using two transport schemes is to illustrate the test cases for both ‘Lagrangian-type’ schemes, that require the approximation of parcel trajectories, and ‘Eulerian-type’ transport schemes. It is not the scope of this paper to compare the specific DG and SL transport schemes. Before discussing the simulations we briefly describe the DG and SL transport schemes used herein.

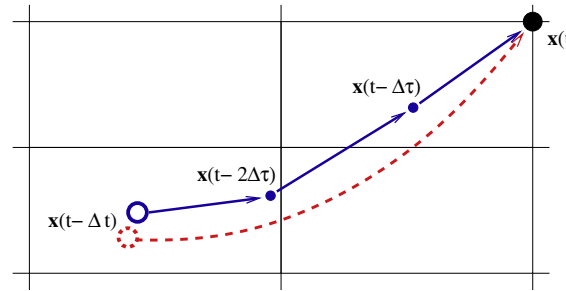


**Fig. 5.** A schematic showing the trajectory computation where the trajectory over  $\Delta t$  is split into  $m = 3$  sub-trajectories that each cover a fractional time step of  $\Delta\tau = \Delta t/m$  (solid arrows). Each trajectory-segment is computed with the Taylor series expansion approach. The arrival point is  $x(t)$  (filled circle), the departure point is  $x(t - \Delta t)$  (unfilled circle) and the intermediate trajectory points are  $x(t - \Delta\tau)$  and  $x(t - 2\Delta\tau)$  (small filled circles). The exact trajectory and departure point are shown with dashed arrow and circle, respectively.

#### 4.1. The DG transport scheme

Specific details of the third-order DG scheme (DG3) considered here are discussed in [Appendix A](#). The time integration is based on a third-order Runge–Kutta Method, and the DG scheme does not use any limiters or filters. The DG scheme is based on the transport Eq. [\(2\)](#). In addition, we also show solutions to the divergent test case 3 using the forced transport Eq. [\(3\)](#). When using the latter configuration we refer to the simulation as ‘Case-3 (Div-free)’. Using [\(2\)](#) for the DG scheme without solving for fluid density implicitly assumes  $\rho$  is everywhere unity at the end of the simulation  $\rho(t = 0) = \rho(t = T) = 1$ .

There are  $6N_e^2$  elements on the cubed-sphere which span the entire spherical surface, where  $N_e$  is the number of elements in each coordinate direction on a cube face. The *equivalent* resolution of the cubed-sphere with respect to the regular latitude–longitude sphere at the equator may be approximated as  $90^\circ/(N_e(N_g - 1))$ , where  $N_g$  is the number of Gauss–Lobatto–Legendre (GLL) quadrature points used in any coordinate direction of the element. For the DG3 scheme,  $N_g = 4$  and the approximate equivalent resolution is  $30^\circ/N_e$  (see [Appendix A](#)). In all simulations shown here with the DG transport scheme, 2400 cubed-sphere elements ( $N_e = 20$ ) are used and each element consists of  $4 \times 4$  GLL quadrature points resulting in approximately  $1.5^\circ$  resolution at the equator. The time step used is  $\Delta t = 5/2400$ , or equivalently, 2400 iterations are required for the full simulation until  $T = 5$  units. The time steps used for the DG simulations are sub-optimal, lower than that needed for the Courant–Friedrichs–Lowy (CFL) stability requirement [\[40\]](#).

#### 4.2. Conservative semi-Lagrangian scheme (CSLAM)

A new conservative SL transport scheme ‘CSLAM (conservative semi-Lagrangian multi-tracer transport scheme)’ [\[41\]](#) on the cubed-sphere is also used for demonstrating the deformational tests using a scheme based on characteristics. The CSLAM scheme belongs to the family of inherently conservative *cell-integrated semi-Lagrangian* methods [\[31\]](#), which combine finite-volume and SL methods. CSLAM requires the knowledge of backward trajectories for the cell vertices. On the surface of the sphere, the upstream cells (quadrilaterals) are approximated with great-circle arcs. The CSLAM scheme is based on a geometrically flexible and fully two-dimensional method, and has options for enforcing monotonicity. In order to apply CSLAM on the cubed-sphere, each of its six faces is partitioned into  $N_c^2$  cells (control volumes). There are  $6N_c^2$  cells on the cubed-sphere, and the equivalent resolution with respect to the regular latitude–longitude sphere at the equator is approximately  $90^\circ/N_c$ .

The CSLAM scheme implementation used here is based on the coupled system of equations for  $\rho$  [\(1\)](#) and  $\rho\phi$  [\(2\)](#). The separate numerical solution to the equation for  $\rho$  and  $\rho\phi$  using the CSLAM scheme is described in detail in [\[41\]](#). However, the coupling between the two equations is not discussed in [\[41\]](#). To obtain monotonicity for  $\phi$ , mass-conservation, and consistency between tracer and air mass simultaneously, care must be taken on how the Eqs. [\(1\)](#) and [\(2\)](#) are coupled. A suggestion for a simple coupling satisfying these requirements is given in [Appendix B](#). CSLAM solves the coupled system of Eqs. [\(1\)](#) and [\(2\)](#) even for the non-divergent test cases.

For the CSLAM simulations, we use a spatial resolution with  $N_c = 60$  along each side of the cubed-sphere panel corresponding to approximately  $1.5^\circ$  resolution (unless stated explicitly otherwise). Since CSLAM allows for long time-steps we use two  $\Delta t$ ’s, one that results in ‘large’ CFL numbers throughout the simulation ( $\Delta t = T/120$ ) and one that restricts CFL to approximately unity or less ( $\Delta t = T/600$ ). As justified below, the trajectories are computed with  $m = 10$  where each segment is computed using Taylor series that are  $\mathcal{O}[(\Delta t)^3]$  (the Taylor series formulas for each segment are given in [Section 3.3](#)).

#### 4.3. Results and discussion

We do not show figures for the same simulations using both schemes as the purpose of the numerical simulations is to illustrate the test cases rather than comparing transport schemes. In general, we use the DG scheme to illustrate solutions and use CSLAM to illustrate monotonicity preservation with the deformational non-divergent and divergent flows. Note that the two schemes are discretized using different forms of the transport equations.

**Table 1**

Normalized errors for  $\phi$  for different deformational test cases using quasi-smooth initial conditions (with  $b = 0.1$  and  $c = 1$ ) when using the DG transport scheme. The third-order DG scheme uses 2400 time steps for simulation with total simulation time  $T = 5$  units. The equivalent resolution at the equator (with  $N_c = 20$ ) is  $1.5^\circ$  approximately. '(Div-free)' refers to the DG scheme based on the forced transport Eq. (3) whereas the other simulations are for the DG scheme based on (2) and assuming  $\rho(t = T) = 1$ .

Experiment	$\ell_1$	$\ell_2$	$\ell_\infty$	$\phi_{\max}$	$\phi_{\min}$
Case-1 (non-div)	0.0071	0.0124	0.0216	-0.0004	-0.0175
Case-2 (non-div)	0.0080	0.0139	0.0220	-0.0005	-0.0208
Case-3 (div)	0.0031	0.0048	0.0173	-0.0005	-0.0105
Case-3 (div-free)	0.0024	0.0045	0.0163	-0.0005	-0.0109
Case-4 (Case-2 + SB)	0.0330	0.0562	0.1047	-0.0678	-0.0846

#### 4.3.1. Non-divergent cases

Figs. 1–4 show the initial conditions and DG numerical solutions for Cases 1–4, respectively. The upper panels in Figs. 1–4 show the initial wind fields and the quasi-smooth initial  $\phi$  distributions. The lower panels show numerical solutions at half-time ( $t = T/2$ ) and the final time  $t = T$ , respectively. The extreme deformation of the initial fields occurs at  $t = T/2$ . The standard error norms (defined in Appendix C) for the DG scheme are given in Table 1. The DG3 scheme is not a non-oscillatory scheme (no filter or limiter is used) and the numerical simulation with DG3 results in oscillatory solutions as seen in Figs. 1–4. For many practical applications monotonic solutions are required, and usually a monotonic limiter/filter is used to control or eliminate spurious oscillations [42].

For the non-divergent tests (Case-1 and 2), the cosine-bells (13) move away from the initial positions and deform into thin crescent (Case-1) or spiral (Case-2) shapes at time  $t = T/2$ . The trajectories are non-trivial (i.e., not the great-circle tra-

**Table 2**

Same as Table 1 but for the CSLAM scheme using 120 and 600 time-steps for the simulation, respectively. Also, the approximate maximum CFL number of the two coordinate directions (locally on each panel) is shown. The trajectories were approximated using three segments ( $m = 3$ ) where each segment was computed using third-order Taylor series expansions. The CSLAM solution for  $\phi$  is based on the coupled system of equations, (1) and (2), as outlined in Appendix A.

Experiment	Max CFL	Time steps	$\ell_1$	$\ell_2$	$\ell_\infty$	$\phi_{\max}$	$\phi_{\min}$
Case-1 (non-div)	3.9	120	0.0062	0.0136	0.0257	-0.0018	-0.0172
Case-1 (non-div)	0.8	600	0.0097	0.0206	0.0348	-0.0024	-0.0208
Case-2 (non-div)	3.7	120	0.0115	0.0246	0.0347	-0.0067	-0.0213
Case-2 (non-div)	0.7	600	0.0134	0.0278	0.0358	-0.0119	-0.0250
Case-3 (div)	1.1	120	0.0045	0.0102	0.0239	-0.0046	-0.0018
Case-3 (div)	0.2	600	0.0046	0.0101	0.0212	-0.0037	-0.0114
Case-4 (non-div)	5.5	120	0.0158	0.0328	0.0473	-0.0068	-0.0214
Case-4 (non-div)	1.1	600	0.0533	0.1088	0.1421	-0.1328	-0.0488

**Table 3**

Normalized errors for  $\phi$  for test case 4 (using quasi-smooth scalar field;  $b = 0.1$  and  $c = 0.9$ ) with the CSLAM transport scheme. The parcel trajectories are divided into  $m$  segments (second column) where each segment is computed using the Taylor series method with formal order of accuracy given in column 1. Time-step ( $\Delta t = T/120$ ) and resolution ( $N_c = 60$  corresponding to approximately  $1.5^\circ$ ) are chosen such that the maximum CFL number in each coordinate direction (locally on each panel) is approximately 5.

Trajectory order	$m$	$\ell_1$	$\ell_2$	$\ell_\infty$
2	1	0.4522	0.9901	0.9111
2	10	0.0627	0.1509	0.1692
2	100	0.0184	0.0365	0.0438
2	1000	0.0159	0.0329	0.0466
2	10000	0.0158	0.0328	0.0469
3	1	0.0185	0.0390	0.0657
3	10	0.0158	0.0328	0.0473
3	100	0.0158	0.0328	0.0470
3	1000	0.0158	0.0328	0.0470
4	1	0.0196	0.0343	0.0567
4	10	0.0159	0.0328	0.0472
4	100	0.0158	0.0328	0.0470
4	1000	0.0158	0.0328	0.0470
5	1	0.0165	0.0341	0.0526
5	10	0.0158	0.0328	0.0472
5	100	0.0158	0.0328	0.0470
5	1000	0.0158	0.0328	0.0470

jectories as used in benchmark transport tests [18,19]) and the cosine-bells pass along the edges and corners covering the six faces of the cubed-sphere. Since the DG scheme does not apply any monotone limiting/filtering non-physical oscillations are present in the numerical solutions.

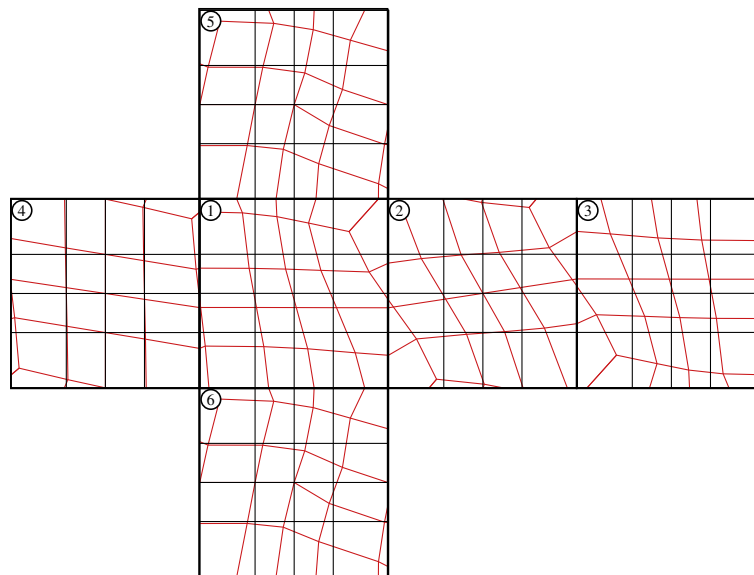
The proposed test case can, of course, be used on any global spherical grid. For example, on a regular latitude-longitude grid the polar cap is usually of special interest and the flow could be rotated to direct flow over the polar regions using a rotated coordinate system [19]. On an icosahedral grid, flow over the 12 pentagons may be of special interest.

Fig. 4 shows the result with Case-2 combined with zonal background flow defined by (29) and (30), that is, Case-4. The zonal background flow challenges the problem further and prevents possible error cancellations when the flow reverses. As can be seen in Table 1, the standard error norms for Case-4 are significantly higher than those for Case-2. This test case configuration is particularly challenging since the distributions at half time ( $t = T/2$ ) are stretched into thin filaments and these are being translated with the zonal wind at the same time. In Table 2, the corresponding error norms for the CSLAM scheme are given using a 'long' and shorter time-step. In general, the error norms worsen with a shorter time-step for the CSLAM scheme which is likely to be a result of the increased number of remappings needed for the shorter time-step simulation as well as the fact that dispersion and damping properties vary as a function of CFL number [43].

Since the trajectories are not known analytically, we assess the accuracy of the Taylor series method using test Case-4 that probably has the most challenging trajectories of the four test case configurations considered here. Also, we use a resolution and time-step that results in a ('extreme') maximum CFL number of approximately 5 in each coordinate direction (locally on each cube panel). Table 3 shows standard error measures using  $m$  trajectory segments based on 2nd, 3rd, 4th, or 5th order Taylor series. Error norms  $l_1$ ,  $l_2$  and  $l_\infty$  converge to the same value when using a high enough value of  $m$  except for the  $l_\infty$  error norm when using second-order trajectories for which there seem be some cancellation of errors for  $m = 100$  and  $m = 1000$ . For third and higher-order trajectory segments all error norms have converged to at least 3 digits when using a value of  $m = 10$  or higher. We therefore conclude that using 10 segments where each segment is 3rd-order provides practically *analytical* trajectories in terms of convergence of the standard error norms. As mentioned earlier, this configuration ( $m = 10$  with third-order segments) is used for trajectory computations in this paper.

Since high-order accurate numerical trajectories can be generated using the Taylor series expansion method outlined above, the test cases considered here can also be used for testing the accuracy of trajectory algorithms used for global SL schemes. Even for a relatively smaller CFL number, the upstream Lagrangian mesh, that ends up at the regular Eulerian grid after one  $\Delta t$ , is considerably deformed as shown in Fig. 6 for test Case-1. Thus, the deformational flow tests presented here provide a challenging test suite for SL schemes.

To test schemes for monotonicity preservation, it is convenient to use a non-smooth initial condition such as the slotted-cylinder initial condition defined in Section 3.1.3 (see Fig. 7). Perhaps the most challenging flow in which to place the discontinuous initial condition (in terms of the diffusive properties usually associated with filter/limiters) is Case-4 since at the point of extreme deformation the slotted-cylinders have deformed into thin filaments that are transported with the zonal background flow.



**Fig. 6.** The static Eulerian grid (thin lines aligned with coordinate lines) and departure grid (deformed thin lines) at the first time-step shown on the gnomonic projection on each cubed-sphere panel for test case 1 with a time-step of  $T/40$  and spatial resolution  $N_c = 4$  (maximum CFL locally on each panel is approximately 0.8). The departure grid has been constructed by computing trajectories for the cell vertices and then the vertices are connected with straight lines.

### 4.3.2. Divergent cases

Numerical simulations in a divergent flow environment is more complex than the non-divergent case and requires special attention. In a non-divergent case and assuming  $\rho(t=0) = 1$ , the continuous transport Eqs. (1) and (2) reduce to a single Eq. (6) as the analytic solution to (1) is trivial  $\rho(t=0) = \rho(t) = 1$ . Consequently, one only needs to solve one continuity equation for the evolution of  $\phi$  if one assumes that the numerical scheme will preserve a constant initial condition for density  $\rho$  (which is not necessarily the case). We also note that under divergent flow conditions  $\rho\phi$  can take values that are not in the interval  $[\min(\rho(t=0)\phi(t=0)), \max(\rho(t=0)\phi(t=0))]$  whereas  $\phi$  should remain in the interval  $[\min(\phi(t=0)), \max(\phi(t=0))]$  throughout the simulation. Moreover, if  $\phi(t=0) = \phi_0$  it should remain constant throughout the simulation (even when the flow is divergent) and if solving the coupled system of Eqs. (1) and (2) the numerical solution to (2) should reduce to the numerical solution to (1). The latter is regarded an important consistency requirement in atmospheric modeling. The domain conserved quantities are fluid density  $\rho$  and tracer density  $\rho\phi$  but not  $\phi$ . The mixing ratio or concentration  $\phi$  is only preserved along parcel trajectories (4).

The divergent flow test (Case-3) provide flow situations where the symmetrically distributed tracer density field  $\rho\phi$  at  $t=0$  rapidly varies as the flow deforms. We provide numerical simulations for this case using the CSLAM and DG3 schemes. As mentioned before our implementation of CSLAM solves the coupled system of equations for air density and tracer density. At  $t=0$  we set  $\rho(t=0) = 1$  as for all other test cases. The value of  $\phi$  can be extracted from the numerical solution for  $\rho$  and  $\rho\phi$  at any time during the simulation as in the case of a practical application (see Appendix B).

Since, (3) is directly derived from the system (1) and (2), the mixing ratio  $\phi$  can be solved from the forced transport Eq. (3). However, recall that  $\rho\phi$  is not necessarily a conservative quantity when using this option. We employ the DG3 scheme to solve the forced transport Eq. (3) with cosine-bells as the initial scalar field. The results with this test are given in Table 1 and denoted “Div-free”.

Another option for the divergent flow test (Case-3) is to solve only the conservation law (2) rather than solving the coupled system (1) and (2). However, in this case the initial and final value of  $\rho$  is assumed to be 1, and the conserved quantity evolving in time is tracer density  $\rho\phi$ . We use DG3 scheme to solve (2) with the scalar fields (13) and (16). In Case-3 (Fig. 3), the initial peak value of the tracer density ( $\rho\phi$ ) field is 1. However, at time  $t=T/2$  this increases up to 3.245 in a narrow band

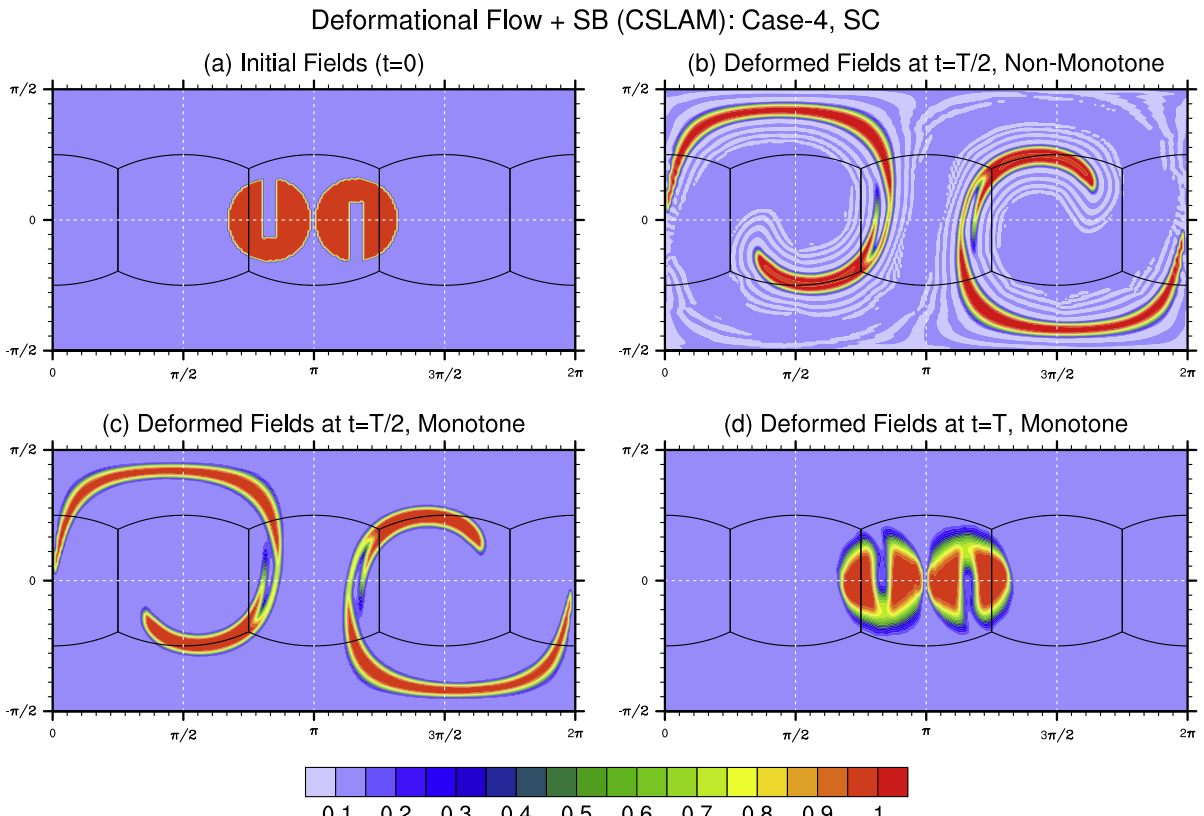


**Fig. 7.** Contour plots of the mixing ratio fields  $\phi$  for the non-divergent deformational flow field Case-2 with background zonal wind (Case-4) with slotted-cylinder initial conditions for  $\phi$  at an approximate resolution of  $1.5^\circ$  along the equator at time  $t=0$  (a),  $t=T/2$  (b and c) and  $t=T$  (d), respectively, computed with CSLAM without any filters (b) and with a monotone reconstruction function filter (2nd row). The simulation was completed in 120 time-steps, resulting in a maximum CFL number of 5.5 in each coordinate direction locally on each panel.

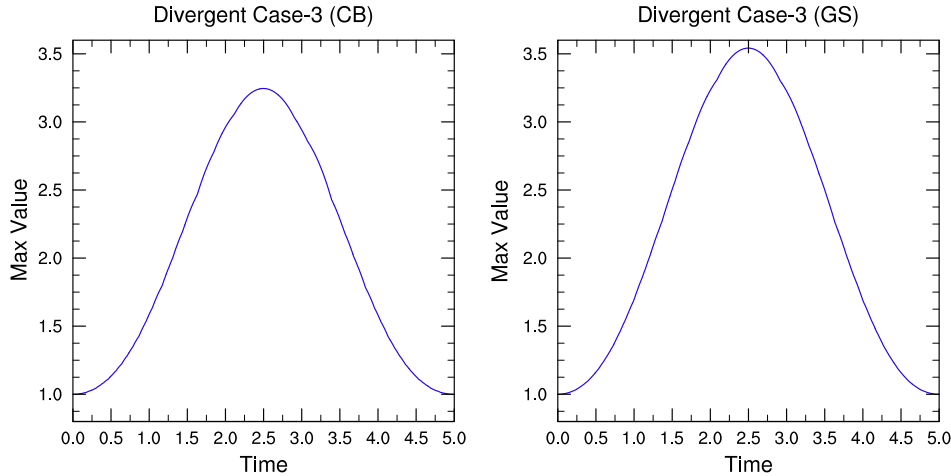


**Fig. 8.** Maximum value of tracer density  $\rho_\phi$  as a function time in the divergent flow (Case-3). The left panel shows the case for which two cosine-bells (13) are used as initial condition. The right panel shows the solution for the smooth case where a Gaussian function (14) is used as the initial condition. The equivalent resolution at the equator (with  $N_e = 20$ ) for these tests is  $1.5^\circ$  approximately.

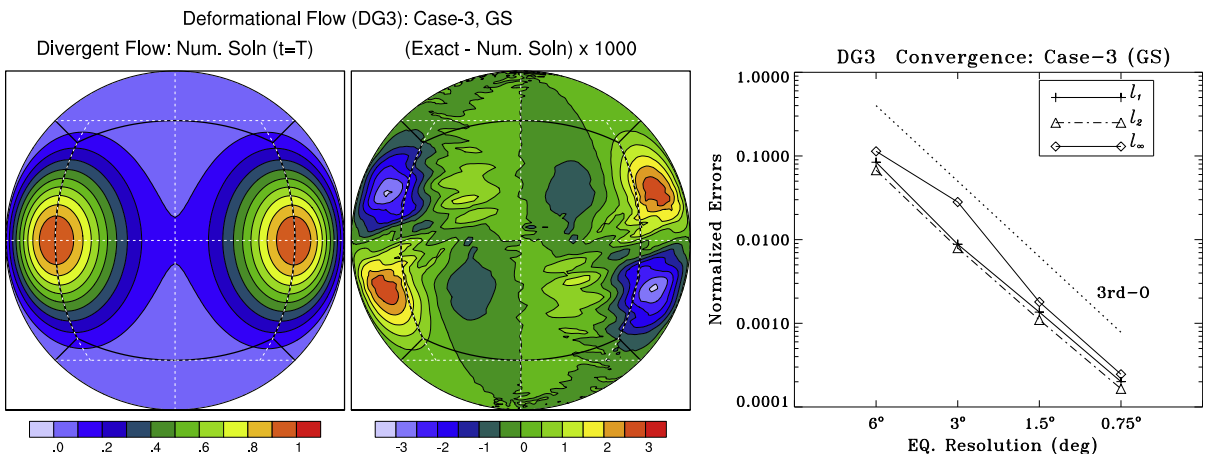
as shown in Fig. 3(c). The maximum value of the tracer density field as a function of time is shown in Fig. 8 for the quasi-smooth cosine-bells (13) and a smooth Gaussian function (14) in the left and right panels, respectively. The maximum value for the Gaussian function (Fig. 8, right panel) at a resolution  $1.5^\circ$  is approximately 3.5445. We have repeated the experiment at a higher resolution ( $0.75^\circ$ ), however, the change in the peak value of  $\rho_\phi$  is not significant, and is approximately 0.0009.

Fig. 9 shows the smooth solution with double Gaussian-hills (14) at time  $t = T$ , where the left and central panels, respectively, show the numerical solution and difference field at a resolution  $1.5^\circ$ . The right panel in Fig. 9 shows the convergence of  $\ell_1$ ,  $\ell_2$  and  $\ell_\infty$  errors for DG3 at various resolutions. The time steps used for the convergence test were chosen such that the time truncation error is negligible. The DG3 scheme exhibits third-order convergence as expected.

Fig. 10 shows the solution to the Case-3 using CSLAM with and without a monotone reconstruction function filter when using slotted-cylinder initial conditions. The divergent flow field provides a challenging environment to test monotonicity constraints under divergent flow conditions. The error norms for Case-3 when using Cosine bell initial conditions with CSLAM are given in Table 3.

#### 4.4. Suggested test case suite

In order to validate new global transport schemes one can perform tests with various combinations of the flow fields and initial scalar distributions. We suggest transport scheme developers to run the following test suite:



**Fig. 9.** Orthographic projection of the numerical solution and the difference field (exact minus numerical) multiplied by 1000 at a resolution  $1.5^\circ$  are shown in the left and central panels, respectively. The initial condition for this test is same as in Case-3 but scalar field used is the smooth double Gaussian hills (16). The right panel shows the convergence of the normalized errors for the DG3 scheme at various equivalent resolutions.

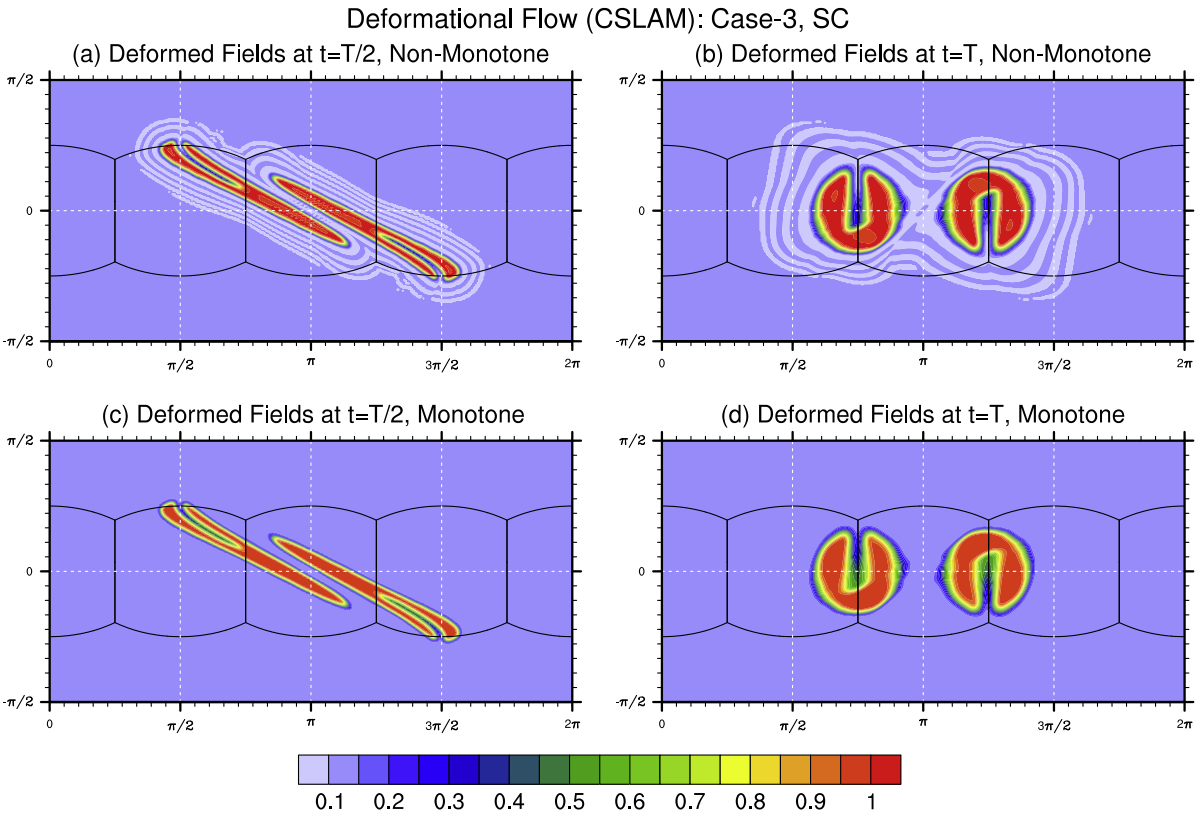


Fig. 10. Same as Fig. 7 but for Case-3.

1. Assess the schemes ability to preserve a non-zero constant density field,  $\rho(t = 0) = \rho_0$ , for non-divergent flows with any of the non-divergent wind fields (for example, Case-4). Test if the scheme is capable of maintaining a non-zero constant concentration,  $\phi(t = 0) = \phi_0$ , in both non-divergent (e.g., Case-4) as well as divergent flows (Case-3).
2. If the coupled system of Eqs. (1) and (2) is used, check for consistency. That is, the numerical solution to (2) should reduce to the numerical solution to (1) when  $\phi(t = 0) = 1$ .
3. Run all test cases with the cosine-bell (13) initial condition with  $b = 0.1$  and  $c = 1$  (Section 3.1.1).
4. To assess monotonicity properties under non-divergent and divergent flow conditions, run Case-3 and Case-4 with the slotted cylinders initial condition (Section 3.1.3).
5. To assess a schemes numerical convergence rate under complex flow conditions run Case-3 (divergent) and Case-4 (non-divergent) using the smooth initial condition (Section 3.1.2) at successively higher resolutions.

## 5. Conclusions

A class of new benchmark deformational flow test cases for horizontal linear transport problems on the sphere have been proposed. The test suite consists of three different initial conditions (smooth, quasi-smooth and non-smooth) placed in either divergent or non-divergent flows. The initial conditions are prescribed in terms regular latitude–longitude coordinates, employing simple trigonometric expressions on a unit sphere. These tests are easy to implement on any type of spherical grid. The transported scalar field follows complex trajectories and undergoes severe deformation during the simulation, reverses its course halfway through the simulation and returns to the initial position by the end of the simulation. This process makes the exact solution available at the end of the simulation and facilitates validation of the underlying transport scheme.

In the context of semi-Lagrangian schemes, these time-varying flow fields can be used to test trajectory algorithms. A scheme for deriving high-order trajectories is provided as well. The divergent flow is specifically aimed to test for conservation and monotonicity (positivity) preservation by limiters/filters in a challenging flow field. The test cases are demonstrated with two different transport schemes on the cubed-sphere, which are based on the discontinuous Galerkin (DG) method and an inherently conservative semi-Lagrangian method (CSLAM). These transport schemes are used to illustrate the characteristics of the test cases. The proposed class of test cases can be used on any type of spherical grid system and with any global transport scheme. The flow field can be oriented in any desired direction on the sphere so that it covers spherical regions of special interest. This is possible by specifying the problem (Cases: 1–4) in a rotated coordinate system.

We anticipate that the proposed class of test cases would complement the existing transport tests and would be a useful tool for testing new transport schemes on a variety of spherical grid systems, new sophisticated numerical methods such as adaptive mesh refinement on the sphere, and testing the accuracy of trajectory algorithms in non-trivial flow fields. We have made several specific recommendations on how this test suite could be used for validating global transport schemes.

## Acknowledgments

The authors are thankful to Dr. Joseph J. Tribbia, Dr. David L. Williamson, Dr. Rashmi Mittal, Dr. Lucas M. Harris, Dr. Christoph Erath, and Dr. Natasha Flyer for internal reviews of the manuscript. Discussions with Dr. Dale Durran, Dr. Mark A. Taylor, and Dr. Oksana Guba are gratefully acknowledged. The authors would like thank three anonymous reviewers for their comments which significantly improved the paper. Authors were partially supported by the DOE BER Program under award DE-SC0001658.

## Appendix A. The DG transport scheme on the cubed-sphere

The discontinuous Galerkin (DG) method may be considered as a hybrid conservative approach combining the nice features of the finite-element and finite-volume methods [40]; and is becoming increasingly popular in atmospheric modeling applications [42]. Here, we briefly outline the DG transport scheme on the cubed-sphere, which is used for the deformational flow simulations. A detailed account of the DG scheme implementation on the cubed-sphere can be found in [44,34,45].

The cubed-sphere geometry consists of partitioning the sphere  $\mathcal{S}$  into six identical regions (faces) based on an equiangular gnomonic projection [39,3] of an inscribed cube. The computational domain is the cube  $\mathcal{C}$  with sides  $x^1, x^2 \in [-\pi/4, \pi/4]$ , and the transport equation can be solved on  $\mathcal{C}$  by the virtue of gnomonic mapping. The Jacobian of the mapping  $\sqrt{G}$  has an explicit analytic form and is identical on each face of the cube [44]. For the DG scheme implementation, each face of the cubed-sphere is further partitioned into  $N_e \times N_e$  non-overlapping rectangular elements such that  $6N_e^2$  elements span the entire spherical surface. For the deformational tests using the DG scheme we employed the transport Eqs. (3) and (6). This can be generalized to the following form on  $\mathcal{C}$ .

$$\frac{\partial \Psi}{\partial t} + \nabla \cdot \mathbf{F}(\Psi) = S(\Psi), \quad \text{in } \mathcal{C} \times (0, T], \quad (47)$$

where  $\Psi = \sqrt{G}\phi$ ,  $\phi$  is a scalar field,  $S$  is the source term and flux vector  $\mathbf{F} = (\Psi u^1, \Psi u^2)$  involves contravariant components  $(u^1, u^2)$  corresponding to the wind vector  $\mathbf{V} = (u, v)$ . The gradient operator  $\nabla \equiv (\partial/\partial x^1, \partial/\partial x^2)$  is defined on  $\mathcal{C}$ .

Since the DG discretization process is identical for each element, we consider only a generic element  $\Omega_e$ . The approximate solution  $\Psi_h$  is assumed to be in a vector space  $\mathcal{V}_h$  of polynomials of degree up to  $N$  such that

$$\mathcal{V}_h = \{\varphi \in L^2(\mathcal{C}) : \varphi|_{\Omega_e} \in \mathcal{P}_N(\Omega_e), \forall \Omega_e \in \mathcal{C}\},$$

where

$$\mathcal{P}_N = \text{span } \{(x^1)^m (x^2)^n : 0 \leq m, n \leq N\}.$$

The weak formulation of the problem can be obtained by multiplying (47) by a test function  $\varphi_h$  in  $\mathcal{V}_h$  and integrating by parts over  $\Omega_e$ . To find the approximate solution  $\Psi_h \in \mathcal{V}_h$  we consider the following semi-discretized weak formulation on each element  $\Omega_e \in \mathcal{C}$  such that,

$$\frac{d}{dt} \int_{\Omega_e} \Psi_h \varphi_h d\Omega - \int_{\Omega_e} \mathbf{F}(\Psi_h) \cdot \nabla \varphi_h d\Omega + \int_{\Gamma_e} \hat{\mathbf{F}} \cdot \mathbf{n} \varphi_h d\Gamma = \int_{\Omega_e} S(\Psi_h) \varphi_h d\Omega, \quad (48)$$

where  $\hat{\mathbf{F}}$  is the numerical flux,  $\mathbf{n}$  is the outward-facing unit normal vector on the element boundary  $\Gamma_e$  and  $d\Omega = dx^1 dx^2$ . For the present study, we employ the local Lax-Friedrichs flux formula:

$$\hat{\mathbf{F}}(\Psi_h) = \frac{1}{2} [(\mathbf{F}(\Psi_h^-) + \mathbf{F}(\Psi_h^+)) - \alpha(\Psi_h^+ - \Psi_h^-)],$$

where  $\alpha$  is the maximum of the absolute value of the velocity components normal to the element boundary  $\Gamma_e$ ;  $\Psi_h^-$  and  $\Psi_h^+$  are, respectively, the left and right limits of  $\Psi_h$  along the boundary  $\Gamma_e$ .

In order to evaluate (efficiently and accurately) the integrals in the weak formulation, as represented in (48), an orthogonal polynomial based basis set is usually employed. The integrals are approximated with a high-order accurate Gauss quadrature rule; this requires a local mapping from  $\Omega_e$  to the reference element  $[1,1]^2$  done by introducing new independent variables  $\xi^i = \xi^i(x^i)$ ,  $i \in \{1,2\}$  such that  $\xi^i \in [-1, 1]$ . The nodal basis set which spans  $\mathcal{V}_h$  is chosen to be a tensor-product of polynomials  $h_k(\xi^1)h_\ell(\xi^2)$ , where  $h_k(\xi^i)$  is the Lagrange-Legendre (orthogonal) polynomial. Now the approximate solution  $\Psi_h$  and test function  $\varphi_h$  in  $\mathcal{V}_h$  can be expanded in terms of a tensor-product of the Lagrange basis functions, and in the case of  $\Psi_h$

$$\Psi_h(\xi^1, \xi^2) = \sum_{k=0}^N \sum_{\ell=0}^N U_h(\xi_k^1, \xi_\ell^2) h_k(\xi^1) h_\ell(\xi^2),$$

where  $\{\xi_\ell^i\}_{i=0}^N$  are  $N_g = N + 1$  Gauss–Lobatto–Legendre (GLL) quadrature points. There are  $N_g \times N_g$  GLL points on the reference element  $[-1, 1]^2$ . Substitution of the expansions for  $\Psi_h$  and  $\varphi_h$  in the weak formulations and further simplification leads to the following ordinary differential equation in time corresponding to the continuous problem (47),

$$\frac{d\Psi_{k\ell}}{dt} = L(\Psi_{k\ell}) \text{ in } (0, T], \quad (49)$$

where  $\Psi_{k\ell}$  are the time dependent nodal (or grid point) values corresponding to  $\Psi_h$ . We use a third-order accurate explicit strong-stability preserving Runge–Kutta time integration procedure [46] for solving (49).

Note that the choice of the GLL quadrature rule is purely based on easy implementation and efficiency considerations. However, the approximation of the integrals in (48) with GLL quadrature results in inexact integration and may degrade the overall accuracy of the DG scheme. We consistently employ  $4 \times 4$  GLL points ( $N_g = 4$ ) on each element so that the resulting “DG3” scheme is formally at least third-order accurate.

## Appendix B. A brief description of CSLAM

The CSLAM forecast for the cell-averaged fluid density and tracer concentration in cell  $k$ ,  $\bar{\rho}_k(t)$  and  $\bar{\phi}_k(t)$  respectively, is derived by integrating (1) and (2) over a Lagrangian area  $A_k(t)$  and discretizing in time and space

$$\bar{\rho}_k(t) = \frac{1}{\Delta A_k(t)} \int_{A_k(t-\Delta t)} \rho(x, y, t - \Delta t) dA \quad (50)$$

$$\bar{\phi}_k(t) = \left\{ \frac{1}{\Delta A_k(t)} \int_{A_k(t-\Delta t)} \rho(x, y, t - \Delta t) \phi(x, y, t - \Delta t) dA \right\} / \bar{\rho}_k(t), \quad (51)$$

where  $A_k(t - \Delta t)$  is the upstream deformed Lagrangian area that ends up at the regular grid cell  $A_k(t) = A_k$  after being transported by the flow one time-step  $\Delta t$  (see Fig. 1 in [41]). The area of the upstream deformed cell and regular Eulerian cell are denoted  $\Delta A_k(t - \Delta t)$  and  $\Delta A_k$ , respectively. The sub-grid-cell reconstruction function of fluid density in cell  $k$  at time  $t - \Delta t$  is based on a fully two-dimensional biquadratic polynomial function

$$\begin{aligned} \rho_k(x, y, t - \Delta t) = & a_k^{(\rho)} + \left( \frac{\partial \rho}{\partial x} \right)_k (x - x_0) + \left( \frac{\partial \rho}{\partial y} \right)_k (y - y_0) + \frac{1}{2} \left( \frac{\partial^2 \rho}{\partial x^2} \right)_k (x - x_0)^2 + \left( \frac{\partial^2 \rho}{\partial x \partial y} \right)_k (x - x_0)(y - y_0) \\ & + \frac{1}{2} \left( \frac{\partial^2 \rho}{\partial y^2} \right)_k (y - y_0)^2, \end{aligned} \quad (52)$$

where the centroids are given by

$$x_0 = \frac{1}{A_k} \int_{A_k} x dA, \quad y_0 = \frac{1}{A_k} \int_{A_k} y dA, \quad (53)$$

and the derivatives  $[\partial^{i+j} \rho / (\partial x^i \partial y^j)]_k$  are approximated from cell average values of  $\rho$  at time  $t - \Delta t$ . To ensure mass-conservation, the constant term  $a_k^{(\rho)}$  is chosen so that the integral of  $\rho_k(x, y, t - \Delta t)$  over  $A_k$  equals the mass in cell  $k$  at time  $t - \Delta t$

$$\bar{\rho}_k(t - \Delta t) \Delta A_k = \int_{A_k} \rho_k(x, y, t - \Delta t) dA, \quad (54)$$

(see Eq. A40 in [47]). Since the reconstruction polynomials are not necessarily continuous across cell borders, the integrals on the right-hand side of (50) and (51) are broken up into integrals over overlapping areas between the regular Eulerian cells  $A_k$  and the deformed areas  $A_k(t - \Delta t)$ . These upstream surface integrals are computed as line integrals. The details on how the reconstruction coefficients and integrals over overlap areas are computed on the cubed-sphere are given in [41,47]. The sub-grid-cell polynomial  $\rho_k(x, y, t - \Delta t)$  can be rendered monotone simply by scaling the subgrid reconstructions in each cell so that their extreme values are no greater than the maximum and minimum of the surrounding cells' average values [48,33].

The sub-grid-cell reconstruction for  $\phi_k(x, y, t - \Delta t)$  is computed exactly as for  $\rho_k(x, y, t - \Delta t)$  using the above procedure based on cell average values of  $\phi$  at time  $t - \Delta t$ . To ensure tracer mass conservation, consistency between tracer mass and air mass, and monotonicity of  $\phi$ , the integrand in (51) must be carefully approximated. For example, simply integrating the product of the two polynomial reconstruction functions may violate tracer mass conservation and result in a fully two-dimensional fourth-degree polynomial (with 16 terms), which may be computationally expensive to integrate. Fitting a biquadratic polynomial directly to the product of the cell average values of  $\rho$  and  $\phi$  instead makes it difficult to enforce strict monotonicity for  $\phi$ .

A simple and efficient way to achieve tracer conservation, consistency and monotonicity within the CSLAM framework, is to replace  $\rho(x, y, t - \Delta t) \phi(x, y, t - \Delta t)$  in (51) with

$$\bar{\rho}_k(t - \Delta t) \phi_k(x, y, t - \Delta t) + \bar{\phi}_k(t - \Delta t) [\rho_k(x, y, t - \Delta t) - \bar{\rho}_k(t - \Delta t)]. \quad (55)$$

This formulation avoids problems with coupling the density and concentration reconstructions when performing monotonicity filtering, and avoids evaluating a fourth-order polynomial. If monotonicity is required, the monotone filter is applied to the reconstruction coefficients of  $\phi(x, y, t)$ . If the tracer concentration is equal to one,  $\phi(t = 0) = 1$ , then the reconstruction function in (55) reduces to  $\rho_k(x, y, t - \Delta t)$  and therefore satisfies the consistency requirement. We note that CSLAM may also be cast in flux-form (FF-CSLAM) which may be advantageous, for example, for enforcing monotonicity [33,27].

### Appendix C. Error measures

If  $\phi = \phi(\lambda, \theta, t)$  is the transported concentration field, then global normalized standard errors are defined by [18]:

$$\begin{aligned} \ell_1 &= \frac{I(|\phi - \phi_T|)}{I(|\phi_T|)}, \\ \ell_2 &= \left[ \frac{I[(\phi - \phi_T)^2]}{I[(\phi_T)^2]} \right]^{1/2}, \\ \ell_\infty &= \frac{\max_{\forall \lambda, \theta} |\phi - \phi_T|}{\max_{\forall \lambda, \theta} |\phi_T|}, \\ \phi_{\max} &= \frac{\max_{\forall \lambda, \theta} (\phi) - \max_{\forall \lambda, \theta} (\phi_T)}{\Delta \phi_0}, \\ \phi_{\min} &= \frac{\min_{\forall \lambda, \theta} (\phi) - \min_{\forall \lambda, \theta} (\phi_T)}{\Delta \phi_0}, \end{aligned}$$

where  $\phi_T, \phi_0$  are, respectively, the true solution and its initial value,  $\Delta \phi_0$  is the difference between maximum and minimum value of the initial condition, and the global integral  $I$  is defined as follows,

$$I(\phi) = \frac{1}{4\pi} \int_0^{2\pi} \int_{-\pi/2}^{\pi/2} \phi(\lambda, \theta, t) \cos \theta d\lambda d\theta.$$

Note that for the CSLAM scheme  $\phi$  is the average density or concentration over grid cell and for the DG scheme  $\phi$  is the point value defined on the GLL grids on each element. The global integral  $I(\phi)$  is approximated by a numerical method consistent with the horizontal discretization of the sphere.

### References

- [1] D. Majewski, D. Liermann, P. Prohl, B. Ritter, M. Buchhold, T. Hanisch, G. Paul, W. Wergen, J. Baumgardner, The operational global icosahedral-hexagonal gridpoint model GME: description and high-resolution tests, *Mon. Weather Rev.* 130 (2002) 319–338.
- [2] H. Tomita, M. Tsugawa, M. Satoh, K. Goto, Shallow water model on a modified icosahedral geodesic grid using spring dynamics, *J. Comput. Phys.* 174 (2001) 579–613.
- [3] C. Ronchi, R. Iacono, P.S. Paolucci, The cubed sphere: a new method for the solution of partial differential equations in spherical geometry, *J. Comput. Phys.* 124 (1) (1996) 93–114.
- [4] X. Peng, F. Xiao, K. Takahashi, Conservative constraint for a quasi-uniform overset grid on the sphere, *Quart. J. Roy. Meteor. Soc.* 132 (2006) 979–996.
- [5] M. Zerroukat, N. Wood, A. Staniforth, SLICE A semi-Lagrangian inherently conservative and efficient transport scheme for transport problems on the sphere, *Quart. J. Roy. Meteor. Soc.* 130 (2004) 2649–2664.
- [6] P. Cheruvu, R.D. Nair, H.M. Tufo, A spectral finite volume transport scheme on the cubed-sphere, *Appl. Numer. Math.* 57 (2007) 1021–1032.
- [7] C. Chen, F. Xiao, Shallow water model on cubed-sphere by multi-moment finite volume method, *J. Comput. Phys.* 227 (2008) 5019–5044.
- [8] M. Taylor, J. Edwards, S. Thomas, R. Nair, A mass and energy conserving spectral element atmospheric dynamical core on the cubed-sphere, *J. Phys.: Conf. Ser.* 78, doi:10.1088/1742-6596/78/1/012074.
- [9] F.X. Giraldo, Lagrange–Galerkin methods on spherical geodesic grids: the shallow water equations, *J. Comput. Phys.* 160 (2000) 336–368.
- [10] R.D. Nair, S.J. Thomas, R.D. Loft, A discontinuous Galerkin global shallow water model, *Mon. Weather Rev.* 133 (2005) 876–888.
- [11] N. Flyer, G.B. Wright, Transport schemes on a sphere using radial basis functions, *J. Comput. Phys.* 226 (2007) 1059–1084.
- [12] N. Flyer, G.B. Wright, A radial basis function method for the shallow water equations on a sphere, *Proc. Roy. Soc. A* 465 (2009) 1949–1976.
- [13] C. Jablonowski, M. Herzog, J.E. Penner, R.C. Oehmke, Q.F. Stout, B. van Leer, K.G. Powell, Block-structured adaptive grids on the sphere: advection experiments, *Mon. Weather Rev.* 134 (2006) 3691–3713.
- [14] M. Läuter, D. Handorf, N. Rakowsky, J. Behrens, S. Frickenhaus, M. Best, K. Dethloff, W. Hiller, A parallel adaptive barotropic model of the atmosphere, *J. Comput. Phys.* 210 (2007) 535–553.
- [15] A. St-Cyr, C. Jablonowski, J.M. Dennis, H.M. Tufo, S.J. Thomas, A comparison of two shallow water models with nonconforming adaptive grids, *Mon. Weather Rev.* 136 (2008) 1898–1922.
- [16] P.H. Lauritzen, C. Jablonowski, M.A. Taylor, R.D. Nair, Rotated versions of the Jablonowski steady-state and baroclinic wave test cases: a dynamical core intercomparison, *J. Adv. Model. Earth Syst. – Discuss. (JAMES)* (in press).
- [17] C. Jablonowski, D.L. Williamson, A baroclinic instability test case for atmospheric model dynamical cores, *Quart. J. Roy. Meteor. Soc.* 132 (2006) 2943–2975.
- [18] D.L. Williamson, J.B. Drake, J.J. Hack, R. Jakob, P.N. Swarztrauber, A standard test set for numerical approximations to the shallow water equations in spherical geometry, *J. Comput. Phys.* 102 (1992) 211–224.
- [19] R.D. Nair, C. Jablonowski, Moving vortices on the sphere: a test-case for horizontal advection problems, *Mon. Weather Rev.* 136 (2008) 699–711.
- [20] R.D. Nair, B. Machenhauer, The mass-conservative cell-integrated semi-Lagrangian advection scheme on the sphere, *Mon. Weather Rev.* 130 (2002) 649–667.

- [21] P.K. Smolarkiewicz, The multi-dimensional Crowley advection scheme, *Mon. Weather Rev.* 110 (1982) 1968–1983.
- [22] C.A. Doswell, A kinematic analysis associated with a nondivergent flow, *J. Atmos. Sci.* 41 (1984) 1242–1248.
- [23] A. Staniforth, J. Coté, J. Pudickiewicz, Comments on Smolarkiewicz's deformational flow, *Mon. Weather Rev.* 115 (1987) 894–900.
- [24] R.J. LeVeque, High-resolution conservative algorithms for advection in incompressible flow, *SIAM J. Numer. Anal.* 33 (2) (1996) 627–665.
- [25] P.J. Rasch, Conservative shape-preserving two-dimensional transport on spherical reduced grid, *Mon. Weather Rev.* 122 (1994) 1337–1350.
- [26] P. Jöckel, R. von Kuhlmann, M.G. Lawrence, B. Steil, C. Brenninkmeijer, P.J. Crutzen, P.J. Rasch, B. Eaton, On a fundamental problem in implementing flux-form advection schemes for tracer transport in 3-dimensional general circulation and chemistry transport models, *Q.J.R. Meteorol. Soc.* 127 (573) (2001) 1035–1052.
- [27] P.H. Lauritzen, P.A. Ullrich, R.D. Nair, Atmospheric transport schemes: desirable properties and a semi-Lagrangian view on finite-volume discretizations, in: P.H. Lauritzen, R.D. Nair, C. Jablonowski, M. Taylor (Eds.), *Numerical Techniques for Global Atmospheric Models*, Lecture Notes in Computational Science and Engineering, vol. 80, Springer, in press.
- [28] J.K. Dukowicz, J.R. Baumgardner, Incremental remapping as a transport/advection algorithm, *J. Comput. Phys.* 160 (2000) 318–335.
- [29] D.R. Durran, *Numerical Methods for Wave Equations in Geophysical Fluid Dynamics*, Springer, 1999, p. 465, ISBN 0-387-98376-7.
- [30] W.C. Skamarock, Positive-definite and monotonic limiters for unrestricted time-step transport schemes, *Mon. Weather Rev.* 134 (2006) 2241–2250.
- [31] B. Machenhauer, E. Kaas, P. Lauritzen, Special Volume on Computational Methods for the Ocean and Atmosphere, vol. 14, Elsevier, 2009, pp. 3–120, ISBN-13 978-0-444-51893-4 (Chapter: Finite Volume Methods in Meteorology).
- [32] P.N. Blossey, D.R. Durran, Selective monotonicity preservation in scalar advection, *J. Comput. Phys.* 227 (2008) 5160–5183.
- [33] L.M. Harris, P.H. Lauritzen, A flux-form version of the conservative semi-Lagrangian multi-tracer transport scheme (CSLAM) on the cubed sphere grid, *J. Comput. Phys.* (2010), submitted for publication.
- [34] M.N. Levy, R.D. Nair, H.M. Tufo, High-order Galerkin method for scalable global atmospheric models, *Comput. Geosci.* 33 (2007) 1022–1035.
- [35] S.T. Zalesak, Fully multidimensional flux-corrected transport algorithms for fluids, *J. Comput. Phys.* 31 (1979) 335–362.
- [36] R.D. Nair, J.S. Scroggs, F.H.M. Semazzi, A forward-trajectory global semi-Lagrangian transport scheme, *J. Comput. Phys.* 190 (2003) 275–294.
- [37] J. Coté, M. Roch, A. Staniforth, L. Fillion, A variable-resolution semi-Lagrangian finite-element global model of the shallow water equations, *Mon. Weather Rev.* 121 (1993) 231–243.
- [38] U. Amato, M. Carfora, Semi-Lagrangian treatment of advection on the sphere with accurate spatial and temporal approximations, *Math. Comput. Model.* 32 (2000) 981–995.
- [39] R. Sadourny, Conservative finite-difference approximations of the primitive equations on quasi-uniform spherical grids, *Mon. Weather Rev.* 100 (1972) 136–144.
- [40] B. Cockburn, C.-W. Shu, The Runge–Kutta discontinuous Galerkin method for convection-dominated problems, *J. Sci. Comput.* 16 (2001) 173–261.
- [41] P.H. Lauritzen, R.D. Nair, P.A. Ullrich, A conservative semi-Lagrangian multi-tracer transport scheme (CSLAM) on the cubed-sphere grid, *J. Comput. Phys.* 229 (2010) 1401–1424.
- [42] R.D. Nair, M.N. Levy, P.H. Lauritzen, Emerging methods for atmospheric numerical modeling, in: P.H. Lauritzen, R.D. Nair, C. Jablonowski, M. Taylor (Eds.), *Numerical Techniques for Global Atmospheric Models*, Lecture Notes in Computational Science and Engineering, vol. 80, Springer, in press.
- [43] P.H. Lauritzen, A stability analysis of finite-volume advection schemes permitting long time steps, *Mon. Weather Rev.* 135 (2007) 2658–2673.
- [44] R.D. Nair, S.J. Thomas, R.D. Loft, A discontinuous Galerkin transport scheme on the cubed-sphere, *Mon. Weather Rev.* 133 (2005) 814–828.
- [45] R.D. Nair, Diffusion experiments with a global discontinuous Galerkin shallow-water model, *Mon. Weather Rev.* 137 (2009) 3339–3350.
- [46] S. Gottlieb, C.W. Shu, E. Tadmor, Strong stability preserving high-order time discretization methods, *SIAM Rev.* 43 (2001) 89–112.
- [47] P.A. Ullrich, P.H. Lauritzen, C. Jablonowski, Geometrically exact conservative remapping (GECoRe): regular latitude–longitude and cubed-sphere grids, *Mon. Weather Rev.* 137 (6) (2009) 1721–1741.
- [48] T. Barth, D. Jespersen, The design and application of upwind schemes on unstructured meshes, in: *Proceedings of the AIAA 27th Aerospace Sciences Meeting*, Reno.